Syncytia Formation Promotes Virus Resistance to Interferon and Neutralizing Antibodies

Tiansheng Li[1], Insung Kang[2], Zhe Hu[1], James Gibbs[1], Chengjin Ye[4], Ivan Kosik[1], Guoli Shi[3], Jaroslav Holly[1], Martina Kosikova[2], Alex Compton[3], Luis Martinez-Sobrido[4], Reed F. Johnson[5], Hang Xie[2], Jonathan W. Yewdell[1,6*]

[1]Cellular Biology Section, Laboratory of Viral Diseases, National Institute of Allergy and Infectious Diseases (NIAID), NIH, Bethesda, MD, USA

[2]Laboratory of Respiratory Viral Diseases, Division of Viral Products, Office of Vaccines Research and Review, Center for Biologics Evaluation and Research, Food and Drug Administration, Silver Spring, MD, USA

[3]HIV Dynamics and Replication Program, Center for Cancer Research, National Cancer Institute (NCI), NIH, Frederick, Maryland, USA.

[4]Texas Biomedical Research Institute, San Antonio, TX, USA.

[5]SARS-CoV-2 Virology Core Laboratory, Division of Intramural Research, National Institutes of Health, Bethesda, MD, USA.

[6]Lead contact

*Correspondence: jyewdell@niaid.nih.gov (J.W.Y)

SUMMARY

SARS-CoV-2, like many viruses, generates syncytia. Using SARS-CoV-2 and S (S) expressing recombinant vesicular stomatitis and influenza A viruses, we show that S-mediated syncytia formation provides resistance to interferons in cultured cells, human small airway-derived air-liquid interface cultures and hACE2 transgenic mice. Amino acid substitutions that modulate fusogenicity in Delta- and Omicron-derived S have parallel effects on viral interferon resistance. Syncytia formation also decreases antibody virus neutralization activity in cultured cells. These findings explain the continued selection of fusogenic variants during SARS-CoV-2 evolution in humans and, more generally, the evolution of fusogenic viruses despite the adverse effects of syncytia formation on viral replication in the absence of innate or adaptive immune pressure.

INTRODUCTION

Many medically important enveloped and non-enveloped viruses induce fusion of infected cells with surrounding cells to generate syncytia: multinucleated giant cells[1]. Though syncytia-forming viruses are frequently selected by propagation in patients or cell lines, this is often paradoxically associated with decreased production of infectious viral progeny [2-4]. In this study, we examine this paradox as exhibited by SARS-CoV-2.

While circulating in billions of humans, SARS-CoV-2 continuously evolves immune evasion variants[5-10]. Much of the variation occurs in the S (S) virion surface glycoprotein, which attaches virus to cells by binding ACE2 and subsequently mediates fusion of viral and cell membranes. S possesses an RXXR furin cleavage site (FCS), whose cleavage generates the S1 and S2 subunits (Fig. 1a). This feature distinguishes SARS-CoV-2 from most related viruses in the Sarbecovirus family, although similar FCSs are present in more distantly related coronaviruses (Fig. 1a)[11,12]. FCS cleavage by furin and/or TMPRSS2 enhances viral entry by promoting fusion with the host cell membrane and enhances syncytia formation in cell cultures and in COVID-19 patients[13-18]. The FCS is strongly selected during SARS-CoV-2 circulation in humans (Fig. 1b and Fig.S1) and is associated with increased pathology[19-24].

Interferons play a central role in limiting viral replication in the initial stages of viral infection, particularly in naïve individuals. Strong evidence exists that interferons are a major factor in controlling COVID-19 [25-27]. Studying the evolutionary selection of the FCS *in vitro* and *in vivo*, we have found a critical role for syncytia formation in evading the anti-viral activity of interferons (IFNs) and Abs (Abs).

RESULTS

FCS Confers Virus Resistance to IFN-β in Cell Culture

To better understand the contribution of the S FCS to viral fitness, we replaced the receptor gene of vesicular stomatitis virus (VSV) with the ancestral SARS-CoV-2 S gene to generate a replication-competent VSV-eGFP-SARS-CoV-2 S virus (referred to as rVSV-S, Fig. S2a). We removed the coding sequence for the S 21-residue C-terminal

ER/GC retention sequence to increase S cell surface expression and incorporation into VSV virions[28,29]. We passaged the initial virus stock (P0) in BHK21 cells expressing human ACE2 (referred to as BHK21-ACE2) for several passages. Sanger sequencing at passage 2 (P2) showed only *wt* virus. We detected a small population of the mutant G2045A, corresponding to an R to Q substitution at position 682 (R682Q) after passage 3 (P3), becoming dominant in P4 and P5, accompanied by G2054A, corresponding to R685H (Fig. S2b).

We next sequenced the S genes of 22 plaque-purified P4 stocks expanded in BHK21-ACE2 or MA104 cells, revealing four FCS loss mutants, R685S, R682W, R685H, and R682Q. Each mutant attained higher titers in BHK21-ACE2 cells than the *wt* virus (Fig. S2c). Next-generation sequencing (NGS) revealed an increasing mutation frequency with passage number in BHK21-ACE2 cells occurring at bases encoding R682 or R685 (Fig. 1c). Extending previous findings of FCS loss during propagation in Vero cells for both VSV-S and SARS-CoV-2[21,28-30], this indicates that FCS substitutions enhance virus replication in BHK21-ACE2 cells. A virus growth competition assay using an increasing mutant to *wt* virus ratio demonstrates positive selection for R685S *vs. wt* virus in BHK21-ACE2, and Vero cells and negative selection in Caco-2 cells (Fig. S2d).

To explore the context-dependent fitness of the FCS, we focused on the R685S mutant. To minimize the effects of possible passenger mutations, we generated stocks of recombinant rVSV and rSARS-CoV-2 fluorescent protein (FP) reporter viruses expressing *wt* or R685S S, confirming viral genome sequence by NGS. After low multiplicity of infection (MOI of 0.01) of Vero cells, R685S-virus replicated faster than *wt* virus in both rVSV and rSARS-CoV-2 systems (Fig. 1d, e) as determined by released virions and microscope-based quantitation of reporter FP expression in either live (rVSV-S) or paraformaldehyde (PFA) fixed cells (for rSARS-CoV-2). Importantly, imaging also showed that the size of R685S infection foci was significantly greater than *wt* S in both SARS-CoV-2 or VSV-S vectors (Fig. S3a to f).

FCS Fitness is IFN-Dependent

We noted that FCS loss is selected by virus passaging in Vero and BHK21 cell lines, which share a deficiency in IFN-secretion[31,32]. We tested the contribution of IFN to FCS evolution by adding IFN-β to Vero cells and infecting the cells 20 h later with *wt* or R685S rVSV-S or rSARS-CoV-2 viruses (Fig. 1f,g). As expected, VSV and SARS-CoV-2 were sensitive to IFN-β treatment, exhibiting at least 80% inhibition of FP-reported infection 24 h post-infection (h.p.i) at the lower IFN-β dose used and >96% inhibition at the higher dose. Importantly, relative to R685S, *wt* S conferred up to 23-fold resistance to IFN-β in VSV and less (up to 1.5-fold), but statistically significant resistance in SARS-CoV-2.

Extending these findings to an IFN secretion-competent cell (A549-ACE2), we used the JAK1/2 kinase small molecule inhibitor Ruxolitinib to block IFN-mediated signaling. For both *wt* VSV and SARS-CoV-2 infections, measuring either infected cell FP signal or released infectious virus, Ruxolitinib enhanced R685S infection to a much greater extent than *wt* infection (Fig. 1h and i).

Taken together, these data support the conclusion that the S FCS confers IFN-β-resistance to VSV and SARS-CoV-2 in cultured cells.

Syncytia evade IFN anti-viral activity

How does the FCS confer resistance to IFN-β anti-viral activity? After 18-20 h IFN treatment, we infected cells with rVSV-S and determined the half maximal inhibitory concentration (IC_{50}) of IFN-β in primary infected cells by *in situ* imaging before the release of virus infection (7 h.p.i)(*wt*, 1.16 pM; R685S, 1.14 pM) (Fig. 2a). Compared with VSV-S, SARS-CoV-2 was slightly less sensitive to IFN-β, but *wt* and R685S exhibited near identical IC_{50} values (2.39 *vs.* 2.13 pM) (Fig. 2b). These findings indicate that the FCS does not affect IFN-β inhibition of initial viral entry in Vero cells.

Rather, we found that the FCS reduces IFN anti-viral activity by favoring syncytia formation. We inferred this initially by overlaying S +EGFP transfected Vero cells with RFP transfected Vero cells. Measuring cell fusion by imaging revealed that maximal cell fusion requires S with a functional FCS (Fig. 2c), extending prior reports [28,29]. To further establish the role of the FCS-mediated fusion in evading IFN, we live-imaged infected

Vero cells to measure rVSV-S dissemination. When we treated cells with IFN-β, *wt* rVSV-S infectious foci enlarged over time, while VSV-R685S foci remained limited to single infected cells, many of which died during imaging (Fig. 2d,e and Fig. S4). With SARS-CoV-2 wt infection (Fig. 2f,g and Fig. S5), we observed much larger infection foci consisting of highly multinucleated cells with higher fluorescence, compared with that in R685S infection, with 0.1 ng/ml IFN-β treatment. These data demonstrate that IFN-β under our tested concentration does not block S-mediated Vero cell syncytia formation.

Comparing no IFN-β to IFN-β treatment in VSV-S infection imaging experiments (Fig. S6a), we observed that IFN-β blocks dissemination to non-adjacent cells, consistent with its entry blockade in single cycle experiments (Fig 2a). Treating Vero cells with IFN-β increased the fusion ratio 24 h.p.i. (defined as the area of syncytia divided by the area of syncytia + single infected cells) 1.5-fold vs untreated cells (90% *vs* 60%) (Fig. S6a). Overlaying cells with agar to prevent diffusion of released virus did not affect the fusion ratio of IFN-β treated cells while reducing the fusion ratio of untreated cells to 35% (Fig. S6a). The IFN-β-mediated fusion ratio increase predominantly reflected increases in the size of individual syncytia (containing more individual cells) rather than the number of syncytia (Fig. 2h, and Supplementary Video 1 to 4). In contrast to VSV-S *wt*, VSV-S R685S virus exhibited few and small syncytia, with or without IFN-β (Fig. 2h and Fig. S6b).

We extended these findings to influenza A virus (IAV) using a single cycle infectious IAV mCherrry reporter virus lacking the HA gene segment whose receptor function is provided by S expressed by a transgene. Mixing IAV-mCherry-infected S-expressing cells with eGFP-transfected uninfected cells lacking the HA receptor gene resulted in S-dependent syncytia formation, which enabled mCherry synthesis in eGFP-expressing cells. R685S disruption of the FCS abrogated syncytia formation and influenza-encoded mCherry synthesis (Fig. 2i).

Together, these results demonstrate that IFN-β inhibits S-mediated cell-free transmission of SARS-CoV-2, VSV, and IAV in Vero cells.

Syncytia Confers SARS-CoV-2 IFN Resistance in Human Primary Small Airway Epithelial Cells

We extended our findings to human primary small airway epithelial cells maintained in an air-liquid interface (ALI), a more biologically relevant system. Since airway epithelia have receptors for type III IFNs, which play an important role in respiratory infections[33], we included IFN-λ2 in experiments. Four d after infecting cells with rSARS-CoV-2, we imaged virus-encoded mCherry as a measure of viral gene expression and determined titers of released virus. In the absence of IFNs, *wt* and R685S virus replicated nearly identically (Fig. 3a). Exposing cells before and after infection to either IFN-β or IFN-λ2 reduced *wt* SARS-CoV-2 replication 2- and 6-fold, respectively, by either criterion. Importantly, both IFNs had a much greater effect on blocking R685S SARS-CoV-2 replication (Fig. 3b,c). Imaging infected cells confirmed syncytia formation by *wt* but not the R685S virus (Fig 3d).

We quantitated the effects of IFN on SARS-CoV-2-induced syncytia using image analysis software. No differences in syncytia ratio were observed after IFN-β treatment at a concentration of 0.2 ng/ml, while a slight increase in syncytia ratio occurred in the IFN-λ2 group compared to the group without IFN treatment. Importantly, SARS-CoV-2 R685S rarely generated syncytia without IFN (Fig. 3e). The nuclei count in each syncytium of *wt* ranged from 3 to more than 8, fitting a Gaussian distribution. IFN-β treatment at a concentration of 0.2 ng/ml did not alter the distribution of nuclei in syncytia. In comparison, IFN-λ2 at a concentration of 10 ng/ml slightly increased the overall syncytia ratio (Fig. 3f), likely because of high dose of IFN-λ2 strongly inhibits cell-free infection and thus increases the syncytia ratio. Overall, this suggests that IFN selectively inhibits non-syncytial infection, favoring syncytia in human small airway epithelial cells, consistent with our results in Vero cells and a previous study[34].

To determine the cell types that are involved in syncytia driven by SARS-CoV-2 infection, we stained for markers of ciliated cells (AcTub), goblet cells (Muc5AC), and basal cells (Cytk5). This revealed that syncytia form between ciliated cells, the primary target for SARS-CoV-2 (67%), ciliated cells and basal cells (29%), ciliated cells and goblet cells (3%), or between all three cell types (1%) (Fig. 3g and Fig. S7a).

We next examined SARS-CoV-2 replication in nasal epithelial ALI cultures. Interestingly, while *wt* SARS-CoV-2 replicated to a similar extent as in small airway ALI cultures (determined by fluorescence intensity and infectious virus released 4 d.p.i, Fig. 3h and Fig. S7b), R685S SARS-CoV-2 virus infectious titers were 86-fold lower in nasal cultures, indicating that R685S replication is attenuated in upper airway epithelial cells, suggesting a more vigorous IFN response in the upper *vs.* lower airway which is in line with previous studies[35].

In Vivo Evidence for SARS-CoV-2 Syncytia as an IFN Virus Escape Strategy

To directly examine the contribution of the FCS to evading IFN anti-viral activity *in vivo*, we intranasally infected K18-hACE2 transgenic mice using conditions leading to viral pneumonia. Consistent with the small airway ALI culture experiments, *wt* and R685S SARS-CoV-2 viruses replicated similarly, as indicated by qPCR measurement of vRNA recovered from the lung (Fig. 3i). Treating mice with intranasal IFN-λ2 on day -1 and +1 d.p.i.[36] reduced *wt* vRNA 16-fold while reducing R685S vRNA 33-fold (Fig. 3i). This trend was also observed, though less dramatically when measuring infectious virions. While R685S virus is present at 4- fold higher levels than *wt* virus in untreated mice, in IFN-λ2 -treated mice it is detected in only 2/11 mice *vs.* 4/11 mice for *wt* virus (Fig. 3j). *Wt* SARS-CoV-2 and R685S infections exhibited similar pulmonary proinflammatory cytokine expression profiles 3 d.p.i., except for an increase in *wt* virus induced IL-5 and IFN-γ (Fig. S8). IFN-λ2 treatment decreased proinflammatory cytokines, consistent with its reduction in virus replication.

These findings support the conclusion that the FCS improves viral fitness *in vivo* by enhancing escape from IFN.

Syncytia Enhance Viral Resistance to Antibody Neutralization

A previous study showed that the FCS confers resistance to virus-neutralizing (VN) antibodies (Abs)[19]. To test the contribution of syncytia formation in this altered neutralization profile in viral infection, we devised an imaging-based assay that uniquely

shows VN activity in real time. We used either Vero-ACE2 cells for rVSV infection or human lung alveolar basal epithelial A549/ACE2/TMPRSS2 (ACE2plusC3) cells for SARS-CoV-2 infection. Both cell lines exhibit enhanced syncytia formation due to transgene-encoded protease overexpression. We tested six potent monoclonal Abs (mAbs) specific for the S receptor binding domain (RBD)[37,38] for their ability to block virus-encoded reporter eGFP or mCherry expression. Abs were mixed with virus before infection and maintained during 20 h infection. Data are expressed as the Ab neutralization dose (ND_{50}) required to reduce the FP signal by 50% relative to the no Ab control. We collected images at 7 and 20 h.p.i. (Fig. S9)

Using rVSV to infect Vero-ACE2 cells, large syncytia formed at 20 h.p.i for *wt* virus and did not develop for R685S virus (Fig.S9a). Abs demonstrated negligible to ~1.6-fold more effective VN against R685S at 7h. VN titers dropped for both viruses 20 h.p.i, but the average decrease is ~4.9-fold higher for *wt* rVSV (Fig. S9b).

Using A549 ACE2plusC3 cells, SARS-CoV-2 *wt* but not R685S forms syncytia between 7 and 20 h.p.i (Fig. S9c). As previously reported, SARS-CoV-2 is more sensitive than rVSV-S to Ab mediated VN, likely related to the lower density of S on virions[39]. As with rVSV, *wt* SARS-CoV-2 was slightly more resistant to VN at 7 h.p.i. VN potency dropped 2.5-fold on average for *wt* virus at 20 h.p.i, remaining constant for R685S virus (Fig. S9d).

The resistance of *wt vs.* R685S to Ab-mediated VN, combined with the time-dependent decrease in Ab potency correlating with syncytia formation, robustly supports the conclusion that syncytia formation enhances S escape from VN activity and is likely to contribute to selecting the FCS in S evolution in immune hosts.

S Variants Confirm Syncytia Mediated IFN-Escape

The rapid evolution of SARS-CoV2 S in humans provides a golden opportunity to test the Correlation between S-mediated syncytia formation and IFN-escape. The Delta S variant and its hallmark P681R substitution induce more and larger syncytia than ancestral S[3]. While the Omicron S variant has been reported to reduce syncytia formation[40], the prevalent P681H substitution in Omicron and Alpha S variants can increase syncytia[41].

To better establish the Correlation between fusogenicity and IFN resistance, we generated S proteins from the Delta and Omicron variants and *wt* S variants with hallmark proximal FCS substitutions P681R and P681H.

We first assessed S mediated-syncytia formation using cells expressing S from a transgene-encoded mRNA linking S to GFP via an IRES. While there were comparable numbers of GFP-expressing transfectants, GFP-positive syncytia were significantly reduced in R685S and Omicron S variants compared to *wt* S (Fig.2c and Fig. S10a). As expected, Omicron's compromised syncytia generation was not due to the P681H substitution, which enhanced syncytia when introduced into *wt* S. Conversely, the P681R substitution from the Delta variant and the Delta S itself significantly increased syncytia, with a four-fold increase in GFP area observed in the Delta S group compared to *wt*.

We extended these findings to rVSV-S infection of Vero cells pretreated with IFN-β (0.1 ng/ml) for 20 h. VSV expressing Delta or P681R S formed larger syncytia than VSV-*wt* S, with the opposite observed for Omicron S (Fig. 4a,b). We repeated this experiment using type I (α and β), II (γ), and III (λ2) IFNs over a wide dose range to determine the IFN IC_{50} for blocking infection as measured by total eGFP reporter fluorescence 20 h.p.i. (Fig. 4c). Among five VSV-S viruses tested, R685S was most sensitive to all three types of IFNs, followed by Omicron, *wt*, P681R and Delta, with this rank order maintained for each IFN tested. We calculated the fusion index (Fig. S10b, number of nuclei present in syncytia/number of individual infected cells) for each IFN and plotted the fusion index against the IC_{50} for the five rVSV-S viruses tested (Fig. 4d). This reveals a highly robust correlation between syncytia formation and IFN IC_{50}, with R^2 values ranging from 0.8127 to 0.9543, consistent with causality.

We repeated this experiment by infecting Vero cells for 36 h (MOI 0.05) with *wt* rSARS-CoV-2 virus and viruses with S replaced by one of the four S tested above. As with rVSV, in cells treated with IFN-β (0.1 ng/ml) relative to *wt* S P681R- and Delta-S viruses generated larger and more intense foci measured either by mCherry reporter expression or staining for SARS-CoV-2 nucleocapsid (N) while Omicron foci were smaller and less intense (Fig. 4e, f). Using Calu-3 human lung epithelial cells treated with higher amounts of IFN-β (0.5 and 2.5 ng/ml), R685S was most sensitive to the IFN, followed by the

Omicron. Interestingly, the *wt* showed the lowest sensitivity compared to the other four S variants (Fig. 4g). Lastly, in A549 ACE2plusC3 cells which has been shown to form strong syncytia upon SARS-CoV-2 infection[42], *wt*-, P681R- or Delta-S rSARS-CoV-2 viruses exhibited robust syncytia formation, while R685S- or Omicron-S viruses displayed minimal syncytia (Fig. S10c). R685S and Omicron viruses displayed similar higher sensitivity to IFN-β and IFN-αthan *wt*, P681R, and Delta (Fig. 4h). ACE2plusC3 cells were much less sensitive to IFN-γ or IFN-λ2 against SARS-CoV-2 infection, but showed a similar difference in S-dependent anti-viral activity (Fig. 4h).

In summary, by examining five different S variants in two viral systems and three cell lines treated with four different IFNs, our results demonstrate a positive correlation between S-dependent syncytia formation and fusogenicity and IFN escape.

S Fusogenicity of Dominant Circulating Variants Increases in a Phase-Dependent Manner

How did SARS-CoV-2 evolution over the past 3 years alter S fusogenicity? We examined S from nine dominant strains by mixing Vero cells transfected with a plasmid encoding dual split protein (DSP) DSP_{1-7} or DSP_{8-11} and transfected the mixed culture with S-expressing plasmids. We measured syncytia formation by the generation of fluorescent eGFP from DSP_{1-7} binding to DSP_{8-11}, quantitating the number of syncytia, syncytial area, and fluorescent intensity. This revealed increased S fusogenicity as WA1 evolved to D614G, Alpha, and Delta variants, with a decrease to below WA1 levels in the original Omicron strain (BA.1) with a gradual steady increase with BA.2, BA4/5, BQ.1 to XBB variant. (Fig. 5a to c). We repeated this experiment using an alternative assay based on syncytia formation between human 293FT cells co-transfected with plasmids expressing pmaxGFP and S and human lung epithelial Calu-3 cells (Fig. 5d). This demonstrated the same pattern, with the major difference being less severe increases in Alpha and Delta fusogenicity, but following the trend of increased fusogenicity (Fig. 5d to f).

Interestingly, plotting fusogenicity *vs.* the median date of variant emergence (Fig.S11) showed an increased fusogenicity of S following SARS-CoV-2 evolution in 2 phases (Fig. 5g). Moreover, linear regression analysis of S fusogenicity in each phase, with the median date, yielded a positive correlation for both assays, with R^2 values ranging from 0.70 to

296 0.91 (Fig. 5h). These data suggest a new model for SARS-CoV-2 evolution, with newly
297 introduced strains with major antigenic changes (WA and Omicron BA.1) with low
298 fusogenicity evolving under adaptive and innate immune pressure to increase
299 fusogenicity.

300

301

302 ## DISCUSSION

303 We have addressed why the FCS has been nearly perfectly maintained in millions of
304 isolates during the first 3 years of SARS-CoV-2 evolution in humans. Previous studies
305 established the critical role of the FCS in SARS-CoV-2 replication in human nasal
306 epithelial cells and ferret transmission [20] and that an intact FCS increases pathogenesis
307 in mice and hamsters [19,21-24].

308 Our findings support the conclusion that the FCS increases SARS-CoV-2 fitness by
309 enhancing syncytia formation, which enables virus to escape IFN-induced virion entry
310 inhibition. In IFN-incompetent cells, *e.g.* Vero cells which cannot secrete IFN, syncytia
311 retard viral replication, resulting in the rapid selection of FCS loss mutants, as reported in
312 many studies[19-21,43]. We show that syncytia enable S-expressing VSV to escape IFN,
313 suggesting a general explanation for selecting syncytia-forming viruses in the presence
314 of IFN pressure. We further demonstrate that syncytia formation reduces the efficiency
315 of VN Abs *in vitro*, consistent with a contribution to FCS fitness in immune hosts. This
316 may be a mass action effect based on the need for Ab to block more S present on infected
317 cells *vs.* virions.

318 SARS-CoV-2 S evolution in humans exhibits a punctuated pattern. Following the
319 December 2019 SARS-CoV-2 introduction into humans, S evolved relatively gradually
320 (though faster than IAV HA, the previous poster virus for antigenic drift). The appearance
321 of Omicron BA.1 in Nov 2021 marked a major acceleration in SARS-CoV-2 evolution with
322 34 S amino acid substitutions compared to circulating strains, more akin to antigenic shift
323 in IAV than antigenic drift. This virus likely evolved in an immunocompromised individual,
324 enabling sequential selection of Ab escape mutants [44-50]. If such an individual were also

deficient in IFN-mediated anti-viral activity, this would greatly favor the selection of less fusogenic viruses, which we show have a selective growth advantage in IFN pathway-compromised cells.

While our study does not directly examine the association between fusogenicity and viral pathogenicity, the SARS-CoV-2 literature suggests a positive correlation. The hallmark substitution P681R in the Delta variant that augments fusogenicity contributes to pathogenicity[3]. The pathogenicity of Omicron BA.1, while attenuated compared to Delta, increases in parallel with fusogenicity with variant evolution [40,51-54].

In conclusion, our findings highlight the crucial role of the S FCS in creating viral syncytia, allowing SARS-CoV-2 to evade both innate and adaptive host immunity. Our observation that IFN escape also applies to rVSV and rIAV engineered to utilize S for viral entry is consistent with a general role for viral syncytia in evading IFN responses likely to apply to other syncytia-forming viruses.

FIGURE LEGENDS

Figure 1 Furin cleavage site confers VSV and SARS-CoV-2 resistance to IFN-β anti-viral activity in cell culture.

a Schematic of SARS-CoV-2 S protein structure(up), signal sequence (SS); N-terminal domain (NTD); receptor-binding domain(RBD); receptor-binding motif(RBM); S1/S2 protease cleavage site/furin cleavage site(S1/S2 FCS); S2' protease cleavage site(S2'); fusion peptide(FP); heptad repeat 1(HR1); central helix(CH); connector domain(CD); heptad repeat 2(HR2); transmembrane domain(TM). Polygenetic tree and alignment of S FCS region sequences from five β coronaviruses (bottom). The conserved two key residues RXXR in FCS and cleaved residue are arrow-headed.

b Mutations at FCS in patient SARS-CoV-2 isolates. Substitution counts at each residue at or near the FCS in ~13.9 million SARS-CoV-2 genome sequences deposited to the GISAID database as of May 26th, 2023.

c Mutation frequency at FCS in passaged recombinant replication-competent rVSV-S virus in BHK21-ACE2 cells. The viral genomes of passage 2 to 4 viral stocks were subjected to next-generation sequencing to identify mutations in the S gene, revealing mutations in only FCS.

d and **e** Vero cells were infected at an MOI of 0.01 by rVSV-S (**d**) (n=3) or rSARS-CoV-2(**e**) (n=3). Fluorescence intensity in infected cells was determined by high-content imaging, and virus titers in infected cell supernatants were quantified by infected cell flow cytometry. Data show mean ± s.d.

f and **g** Sensitivity of *wt* and R685S -bearing viruses to exogenous IFN-β in Vero cells. Cells were treated with IFN-β at 0.05 (left) or 0.1 (right) ng/ml for 20 h prior to infection by rVSV-S (**f**)(n=3) or rSARS-CoV-2(**g**)(n=3) at a MOI of 0.01. After virus inoculation, media were replaced with media containing the same amount of IFN-β. Data show mean ± s.d.

h and **i** Blocking JAK1/2 with Ruxolitilib (ruxo) enhances R685S replication in A549-ACE2 cells. A549-ACE2 cells were treated with 2 μM ruxo for 2 h prior to infection by rVSV-S(**h**) or rSARS-CoV-2(**i**) at MOI of 0.01, with ruxo maintained throughout the infection. Fold change of mean fluorescence intensity (MFI) of infected cells (left) and fold change of titer

in the supernatant (right) were normalized by mock-treated values. n=3, except the left panel of **i**. in which n=4 per group. Data show mean ± s.d.

Statistical analysis was performed using a two-tailed, unpaired t-test with Welch's correction. Results represent two independent experiments except for the result in c, which was performed once. *P < 0.05, **P < 0.01, ***P < 0.001 and ****P < 0.0001; ns, not significant.

Figure 2 Syncytia confer virus resistance to IFN-β anti-viral activity.

a and **b** Effect of exogenous IFN-β to viral entry on *wt* and R685S in rVSV-S (**a**) and rSARS-CoV-2 (**b**) was measured in Vero cells at 7 h.p.i with a MOI of 0.01. Series diluted IFN-β was added to monolayers 20 h prior to inoculation. Data show mean ± s.d (n=3).

c Syncytia mediated by S in Vero cells. Vero cells transfected with S expressed from eGFP-IRES-S mRNA were overlaid to Vero cells transfected with mScarlet-plasmid (RFP) at a ratio of 1:4 and incubated for 18-20 h. Syncytial area as determined by GFP-RFP overlapping pixels. Data show mean ± s.d (n = 3).

d Time-lapse imaging of rVSV-S infection in Vero cells exposed to IFN-β (0.025 ng/ml) 20 h prior to infection, at MOI of 0.04. Scale bar, 250 μm

e The area (left) and fluorescence intensity (right) of infection foci in **d**. Data show mean ± s.e.m (n = 500).

f Representative images of rSARS-CoV-2 *wt* and R685S infections in Vero cells under IFN-β treatment (0.1 ng/ml) at 36 h.p.i. Higher-magnification views of the regions indicated by squares are shown in the right images. Scale bar, 100 μm

g Area (left) and fluorescence intensity (right) of infection foci in **f**. Data show mean ± s.e.m (n = 78-165).

h Syncytia formation of rVSV-S *wt* infection in Vero cells under IFN-β treatment. Representative images at 48 h.p.i. (up), and time-lapse measure of mean area of fused focus (setting: object size>60 μm in Gen5) from 18 h.p.i to 48 h.p.i(bottom) (n = 24 fields per group).

i HA-deficient PR8-mCherry replicates in S-mediated syncytia in Vero cells. The workflow was drawn by BioRender and shown at the top. Representative images are shown at the bottom.

Statistical analysis was performed using a one-way ANOVA with multiple comparisons. ***P < 0.001; ns, not significant. Results are representative of two independent experiments.

Figure 3 FCS confers SARS-CoV-2 resistance to IFNs in human small airway epithelial cells and in hACE2 transgenic mice.

a-c Sensitivity of rSARS-CoV-2 *wt* and R685S to IFNs in small airway epithelial cell in air-liquid interface (ALI) format. Representative images of infection in entire ALI cultures treated with IFN-β (0.2 ng/ml) or IFN-λ2 (10 ng/ml) at 4 d.p.i with 10^4 FFU/culture for inoculation(**a**). Fluorescence Intensity of infected cells treated with PBS (left), IFN-β(middle) or INF-λ2 (right) (**b**, n= 9). Titer of apical wash from infected cells treated with PBS (left), IFN-β (middle) or IFN-λ2 (right) **(c**, n=6). 3 donors for each group. Data show mean ± s.d.

d Representative images of syncytia formation in infected small airway ALI treated with IFN-β (0.2 ng/ml) or IFN-λ2 (10 ng/ml) at 4 d.p.i. ALI was stained with anti-AcTub (ciliated cells, green signal) and counterstained with DAPI (gray signal). The infection by SARS-CoV-2 was shown by mCherry (red signal). Z projection was shown. Scale bar, 5μm.

e Syncytia ratio of rSARS-CoV-2 infection in small airway ALI with IFN treatment at 4 d.p.i. The number of individual infected and syncytial cell nuclei was determined from reconstructed 3D confocal images (syncytia defined as 3 or more nuclei in one infected focus). 28 to 47 fields per group were analyzed. Data show mean ± s.d (n=3).

f The nuclei number per syncytia in rSARS-CoV-2 infected in small airway ALI. Data were fit in Gaussian distribution and shown in mean ± s.d (n=3).

g Cell types present in syncytia. Infected small airway ALI were stained with anti-AcTub (green signal, marker for ciliated cell), anti-Cytk5 (yellow signal, marker for basal cell) and

anti-Muc5A (cyan signal, marker for goblet cell) Abs and counterstained with DAPI (gray signal). Individual syncytia were analyzed to determine cell types in syncytia from 3D reconstructed confocal images. The distribution of cell types in syncytia is shown by the pie chart on right. Scale bar, 5μm.

h Comparison of rSARS-CoV-2 *wt* and R685S replication in primary nasal epithelial cells in ALI format (MucilAir from Epithelix) at 4 d.p.i. Fluorescence intensity of infected cells (left) and virus titer from apical wash (right) are shown. Data show mean ± s.d (n=4).

i-j Viral load of rSARS-CoV-2 *wt* and R685S infection in lung tissue of K18-hACE2 mice with (right) or without (left) IFN-λ2 treatment. Viral RNA copies (**i**) and infectious viral titer in infected lungs (**j**) were shown. Data show a combination of two independent experiments. Data show mean ± s.e.m (n=11). DL, detection limit. Statistical analysis was performed using a two-tailed, unpaired t-test (**b,c,h,i,j**) or one-way ANOVA (**e**) with multiple comparisons. *P < 0.05, **P < 0.01, ***P < 0.001 and ****P < 0.0001; ns, not significant.

Figure 4 Correlation between syncytia formation and IFN resistance.

a IFN-β (0.1 ng/ml) pretreated Vero cells were infected (MOI 0.01) with rVSV-S expressing P681R, Delta or Omicron (BA.1) S at 20 h.p.i. IFN-β (0.1 ng/ml) was maintained through infection.

b As in a, with area (top) and fluorescence intensity (bottom) of individual infection foci measured following infection: *wt* (n=1147), P681R (n=888), Delta (n=1179), Omicron (n=1004). Data show mean ± s.e.m

c Dose titration of indicated IFN-treated cells infected with rVSV- S virus expressing *wt*, R685S, P681R, Delta or Omicron S was determined in Vero cells at 20 h.p.i. Cells were treated by a series of diluted IFNs 18-20 h prior to infection and corresponding IFNs were maintained throughout the infection. Data were fitted using nonlinear regression. Data show mean ± s.d. (n=3).

d Correlation of IC_{50} with fusion index for rVSV-S infected Vero cells. The fusion index was calculated by dividing the nuclei number of syncytia foci by the nuclei number of

individual infected cells. Linear regression was performed to correlate the IC_{50} with the fusion index. Details are described in the Method section.

e and **f** Vero cell infection 36 h.p.i with the rSARS-CoV-2 expressing S indicated. Cells were pretreated for 18-20 h with IFN-β (0.1 ng/ml), which was maintained during the infection, mCherry and staining with anti-nucleocapsid (N) protein antibody were shown to indicate infection foci. The area(top) and fluorescence intensity(bottom) of infection foci in the infection of rSARS-CoV-2 *wt*(n=156), P681R(n=146), Delta(n=149), and Omicron(n=113). Data show mean ± s.e.m.

g IFN-β sensitivity of rSARS-CoV-2 virus bearing *wt*, R685S, P681R, Delta and Omicron S in Calu-3 cells at 24 h.p.i. Cells were treated by IFN 18-20 h prior to infection and corresponding IFN were maintained throughout the infection. Data show mean ± s.d (n=3).

h Dose titration of rSARS-CoV-2 virus bearing *wt*, R685S, P681R, Delta and Omicron S against type I (IFN-α and -β), type II (IFN-γ) and type III (IFN-λ2) IFNs were determined in ACE2plusC3 cells at 24 h.p.i. Cells were treated by a series of diluted IFNs 18-20 h prior to infection and corresponding IFNs were maintained throughout the infection. Nonlinear regression was performed to fit the data. Data show mean ± s.d (n=3).

Statistical analysis was performed using a nonparametric Kruskal-Wallis test (**b,f**) or two-way ANOVA test(**g**) with multiple comparisons. *P < 0.05, **P < 0.01, ***P < 0.001 and ****P < 0.0001; ns, not significant. Results are representative of two independent experiments.

Figure 5 Fusogenicity over the course of SARS-CoV-2 evolution occurs in a phase-dependent manner.

a-c Syncytia formation mediated by S protein from circulating SARS-CoV-2 variants was measured in Vero cells using the GFP dual split protein (DSP) system. Vero cells transfected with DSP_{1-7} were mixed with Vero cells transfected with DSP_{8-11}, then the mixed cells were transfected with S-bearing plasmid. Representative images showing syncytia mediated by S from indicated circulating variants at 24 h.p.i. (**a**). Total GFP

positive area normalized to *wt* S (**b**) and GFP positive individual focus area (**c**) were determined (n=4 wells per group).

d-f Syncytia mediated by S protein from circulating SARS-CoV-2 variants was measured in 293FT and Calu-3 cells. 293FT cells co-transfected with S-and pmaxGFP expression plasmids were overlayed on 100% confluent Calu-3 cells for 24 h. Total GFP positive area normalized to *wt* S (**e**) and GFP positive individual focus area (**f**) were determined (n=4 wells per group).

g and **h** Correlation of fusion rate with median isolation date of each circulating variant in two phases. Two independent assays for measuring cell-cell fusion rate of each S of dominant circulating variants showed an increased fusogenicity of S in 2 phases (**g**). In **h**, the top shows the correlation of variants of *wt*, D614G, Alpha and Delta in phase 1, and the bottom shows Omicron subvariants in phase 2 (**h**).

ACKNOWLEDGMENTS

We thank Zene Matsuda at the Institute of Medical Science (University of Tokyo) for providing dual split protein system: DSP $_{1-7}$ and DSP $_{8-11}$, and Chhing-Wen Chang (University of Massachusetts Chan Medical School) for providing A549plusC3 cell line, Sarah Anzick (RTB, NIAID) for NSG support, Bernard Lafont, Johnson Reed, and Nicole Lackemeyer (NIAID SARS-CoV-2 Virology Core BSL-3 facility), for superb support, training, and assistance.

The Cell Biology Section, Laboratory of Viral Diseases, is supported by the Division of Intramural Research, National Institute of Allergy and Infectious Diseases.

Author contributions

T.L., J.W.Y. conceptualized the study. T.L., designed and performed experiments. I.K., M.K. and H.X. performed in vivo experiments. T.L., Z.H., G.S., analyzed syncytia formation in the infection of cultured epithelial cells in ALI. T.L. and J.H. generated stable cell lines. J.G. performed the analysis of SARS-CoV-2 variants proportion. I.K., A.C. and R.F.J. provided essential recourse and scientific input. C.Y. and L.M-S. provided BAC reverse genetic system for recombinant SARS-CoV-2 generation. T.L. and J.W.Y. wrote the manuscript. J.W.Y. acquired funding. All the authors reviewed and proofread the manuscript.

Competing interests

The authors declare that they have no competing interests.

References

1. Zhong, P., Agosto, L.M., Munro, J.B., and Mothes, W. (2013). Cell-to-cell transmission of viruses. Curr Opin Virol *3*, 44-50. 10.1016/j.coviro.2012.11.004.
2. Cathomen, T., Mrkic, B., Spehner, D., Drillien, R., Naef, R., Pavlovic, J., Aguzzi, A., Billeter, M.A., and Cattaneo, R. (1998). A matrix-less measles virus is infectious and elicits extensive cell fusion: consequences for propagation in the brain. EMBO J *17*, 3899-3908. 10.1093/emboj/17.14.3899.
3. Saito, A., Irie, T., Suzuki, R., Maemura, T., Nasser, H., Uriu, K., Kosugi, Y., Shirakawa, K., Sadamasu, K., Kimura, I., et al. (2022). Enhanced fusogenicity and pathogenicity of SARS-CoV-2 Delta P681R mutation. Nature *602*, 300-306. 10.1038/s41586-021-04266-9.
4. Sterjovski, J., Churchill, M.J., Ellett, A., Gray, L.R., Roche, M.J., Dunfee, R.L., Purcell, D.F., Saksena, N., Wang, B., Sonza, S., et al. (2007). Asn 362 in gp120 contributes to enhanced fusogenicity by CCR5-restricted HIV-1 envelope glycoprotein variants from patients with AIDS. Retrovirology *4*, 89. 10.1186/1742-4690-4-89.
5. Cao, Y., Wang, J., Jian, F., Xiao, T., Song, W., Yisimayi, A., Huang, W., Li, Q., Wang, P., An, R., et al. (2022). Omicron escapes the majority of existing SARS-CoV-2 neutralizing antibodies. Nature *602*, 657-663. 10.1038/s41586-021-04385-3.
6. Carabelli, A.M., Peacock, T.P., Thorne, L.G., Harvey, W.T., Hughes, J., Consortium, C.-G.U., Peacock, S.J., Barclay, W.S., de Silva, T.I., Towers, G.J., and Robertson, D.L. (2023). SARS-CoV-2 variant biology: immune escape, transmission and fitness. Nat Rev Microbiol *21*, 162-177. 10.1038/s41579-022-00841-7.
7. Willett, B.J., Grove, J., MacLean, O.A., Wilkie, C., De Lorenzo, G., Furnon, W., Cantoni, D., Scott, S., Logan, N., Ashraf, S., et al. (2022). SARS-CoV-2 Omicron is an immune escape variant with an altered cell entry pathway. Nat Microbiol *7*, 1161-1179. 10.1038/s41564-022-01143-7.
8. Ulrich, L., Halwe, N.J., Taddeo, A., Ebert, N., Schon, J., Devisme, C., Trueb, B.S., Hoffmann, B., Wider, M., Fan, X., et al. (2022). Enhanced fitness of SARS-CoV-2 variant of concern Alpha but not Beta. Nature *602*, 307-313. 10.1038/s41586-021-04342-0.
9. McCallum, M., Bassi, J., De Marco, A., Chen, A., Walls, A.C., Di Iulio, J., Tortorici, M.A., Navarro, M.J., Silacci-Fregni, C., Saliba, C., et al. (2021). SARS-CoV-2 immune evasion by the B.1.427/B.1.429 variant of concern. Science *373*, 648-654. 10.1126/science.abi7994.
10. McCallum, M., Walls, A.C., Sprouse, K.R., Bowen, J.E., Rosen, L.E., Dang, H.V., De Marco, A., Franko, N., Tilles, S.W., Logue, J., et al. (2021). Molecular basis of immune evasion by the Delta and Kappa SARS-CoV-2 variants. Science *374*, 1621-1626. 10.1126/science.abl8506.

11. Andersen, K.G., Rambaut, A., Lipkin, W.I., Holmes, E.C., and Garry, R.F. (2020). The proximal origin of SARS-CoV-2. Nat Med *26*, 450-452. 10.1038/s41591-020-0820-9.
12. Boni, M.F., Lemey, P., Jiang, X., Lam, T.T., Perry, B.W., Castoe, T.A., Rambaut, A., and Robertson, D.L. (2020). Evolutionary origins of the SARS-CoV-2 sarbecovirus lineage responsible for the COVID-19 pandemic. Nat Microbiol *5*, 1408-1417. 10.1038/s41564-020-0771-4.
13. Xia, S., Lan, Q., Su, S., Wang, X., Xu, W., Liu, Z., Zhu, Y., Wang, Q., Lu, L., and Jiang, S. (2020). The role of furin cleavage site in SARS-CoV-2 spike protein-mediated membrane fusion in the presence or absence of trypsin. Signal Transduct Target Ther *5*, 92. 10.1038/s41392-020-0184-0.
14. Zeng, C., Evans, J.P., King, T., Zheng, Y.M., Oltz, E.M., Whelan, S.P.J., Saif, L.J., Peeples, M.E., and Liu, S.L. (2022). SARS-CoV-2 spreads through cell-to-cell transmission. Proc Natl Acad Sci U S A *119*. 10.1073/pnas.2111400119.
15. Papa, G., Mallery, D.L., Albecka, A., Welch, L.G., Cattin-Ortola, J., Luptak, J., Paul, D., McMahon, H.T., Goodfellow, I.G., Carter, A., et al. (2021). Furin cleavage of SARS-CoV-2 Spike promotes but is not essential for infection and cell-cell fusion. PLoS Pathog *17*, e1009246. 10.1371/journal.ppat.1009246.
16. Braga, L., Ali, H., Secco, I., Chiavacci, E., Neves, G., Goldhill, D., Penn, R., Jimenez-Guardeno, J.M., Ortega-Prieto, A.M., Bussani, R., et al. (2021). Drugs that inhibit TMEM16 proteins block SARS-CoV-2 spike-induced syncytia. Nature *594*, 88-93. 10.1038/s41586-021-03491-6.
17. Buchrieser, J., Dufloo, J., Hubert, M., Monel, B., Planas, D., Rajah, M.M., Planchais, C., Porrot, F., Guivel-Benhassine, F., Van der Werf, S., et al. (2020). Syncytia formation by SARS-CoV-2-infected cells. EMBO J *39*, e106267. 10.15252/embj.2020106267.
18. Bussani, R., Schneider, E., Zentilin, L., Collesi, C., Ali, H., Braga, L., Volpe, M.C., Colliva, A., Zanconati, F., Berlot, G., et al. (2020). Persistence of viral RNA, pneumocyte syncytia and thrombosis are hallmarks of advanced COVID-19 pathology. EBioMedicine *61*, 103104. 10.1016/j.ebiom.2020.103104.
19. Johnson, B.A., Xie, X., Bailey, A.L., Kalveram, B., Lokugamage, K.G., Muruato, A., Zou, J., Zhang, X., Juelich, T., Smith, J.K., et al. (2021). Loss of furin cleavage site attenuates SARS-CoV-2 pathogenesis. Nature *591*, 293-299. 10.1038/s41586-021-03237-4.
20. Peacock, T.P., Goldhill, D.H., Zhou, J., Baillon, L., Frise, R., Swann, O.C., Kugathasan, R., Penn, R., Brown, J.C., Sanchez-David, R.Y., et al. (2021). The furin cleavage site in the SARS-CoV-2 spike protein is required for transmission in ferrets. Nat Microbiol. 10.1038/s41564-021-00908-w.
21. Zhu, Y., Feng, F., Hu, G., Wang, Y., Yu, Y., Zhu, Y., Xu, W., Cai, X., Sun, Z., Han, W., et al. (2021). A genome-wide CRISPR screen identifies host factors that regulate SARS-CoV-2 entry. Nat Commun *12*, 961. 10.1038/s41467-021-21213-4.
22. Liu, S., Stauft, C.B., Selvaraj, P., Chandrasekaran, P., D'Agnillo, F., Chou, C.K., Wu, W.W., Lien, C.Z., Meseda, C.A., Pedro, C.L., et al. (2022). Intranasal delivery of a rationally attenuated SARS-CoV-2 is immunogenic and protective in Syrian hamsters. Nat Commun *13*, 6792. 10.1038/s41467-022-34571-4.

609 23. Sasaki, M., Toba, S., Itakura, Y., Chambaro, H.M., Kishimoto, M., Tabata, K.,
610 Intaruck, K., Uemura, K., Sanaki, T., Sato, A., et al. (2021). SARS-CoV-2 Bearing
611 a Mutation at the S1/S2 Cleavage Site Exhibits Attenuated Virulence and Confers
612 Protective Immunity. mBio *12*, e0141521. 10.1128/mBio.01415-21.
613 24. Lau, S.Y., Wang, P., Mok, B.W., Zhang, A.J., Chu, H., Lee, A.C., Deng, S., Chen,
614 P., Chan, K.H., Song, W., et al. (2020). Attenuated SARS-CoV-2 variants with
615 deletions at the S1/S2 junction. Emerg Microbes Infect *9*, 837-842.
616 10.1080/22221751.2020.1756700.
617 25. Bastard, P., Rosen, L.B., Zhang, Q., Michailidis, E., Hoffmann, H.H., Zhang, Y.,
618 Dorgham, K., Philippot, Q., Rosain, J., Beziat, V., et al. (2020). Autoantibodies
619 against type I IFNs in patients with life-threatening COVID-19. Science *370*.
620 10.1126/science.abd4585.
621 26. Zhang, Q., Bastard, P., Liu, Z., Le Pen, J., Moncada-Velez, M., Chen, J., Ogishi,
622 M., Sabli, I.K.D., Hodeib, S., Korol, C., et al. (2020). Inborn errors of type I IFN
623 immunity in patients with life-threatening COVID-19. Science *370*.
624 10.1126/science.abd4570.
625 27. Zhang, Q., Bastard, P., Effort, C.H.G., Cobat, A., and Casanova, J.L. (2022).
626 Human genetic and immunological determinants of critical COVID-19 pneumonia.
627 Nature *603*, 587-598. 10.1038/s41586-022-04447-0.
628 28. Case, J.B., Rothlauf, P.W., Chen, R.E., Liu, Z., Zhao, H., Kim, A.S., Bloyet, L.M.,
629 Zeng, Q., Tahan, S., Droit, L., et al. (2020). Neutralizing Antibody and Soluble
630 ACE2 Inhibition of a Replication-Competent VSV-SARS-CoV-2 and a Clinical
631 Isolate of SARS-CoV-2. Cell Host Microbe *28*, 475-485 e475.
632 10.1016/j.chom.2020.06.021.
633 29. Dieterle, M.E., Haslwanter, D., Bortz, R.H., 3rd, Wirchnianski, A.S., Lasso, G.,
634 Vergnolle, O., Abbasi, S.A., Fels, J.M., Laudermilch, E., Florez, C., et al. (2020). A
635 Replication-Competent Vesicular Stomatitis Virus for Studies of SARS-CoV-2
636 Spike-Mediated Cell Entry and Its Inhibition. Cell Host Microbe *28*, 486-496 e486.
637 10.1016/j.chom.2020.06.020.
638 30. Sasaki, M., Uemura, K., Sato, A., Toba, S., Sanaki, T., Maenaka, K., Hall, W.W.,
639 Orba, Y., and Sawa, H. (2021). SARS-CoV-2 variants with mutations at the S1/S2
640 cleavage site are generated in vitro during propagation in TMPRSS2-deficient cells.
641 PLoS Pathog *17*, e1009233. 10.1371/journal.ppat.1009233.
642 31. Otsuki, K., Maeda, J., Yamamoto, H., and Tsubokura, M. (1979). Studies on avian
643 infectious bronchitis virus (IBV). III. Interferon induction by and sensitivity to
644 interferon of IBV. Arch Virol *60*, 249-255. 10.1007/BF01317496.
645 32. Emeny, J.M., and Morgan, M.J. (1979). Regulation of the interferon system:
646 evidence that Vero cells have a genetic defect in interferon production. J Gen Virol
647 *43*, 247-252. 10.1099/0022-1317-43-1-247.
648 33. Vanderheiden, A., Ralfs, P., Chirkova, T., Upadhyay, A.A., Zimmerman, M.G.,
649 Bedoya, S., Aoued, H., Tharp, G.M., Pellegrini, K.L., Manfredi, C., et al. (2020).
650 Type I and Type III Interferons Restrict SARS-CoV-2 Infection of Human Airway
651 Epithelial Cultures. J Virol *94*. 10.1128/JVI.00985-20.
652 34. Beucher, G., Blondot, M.L., Celle, A., Pied, N., Recordon-Pinson, P., Esteves, P.,
653 Faure, M., Metifiot, M., Lacomme, S., Dacheux, D., et al. (2022). Bronchial
654 epithelia from adults and children: SARS-CoV-2 spread via syncytia formation and

type III interferon infectivity restriction. Proc Natl Acad Sci U S A *119*, e2202370119. 10.1073/pnas.2202370119.

35. Alfi, O., Yakirevitch, A., Wald, O., Wandel, O., Izhar, U., Oiknine-Djian, E., Nevo, Y., Elgavish, S., Dagan, E., Madgar, O., et al. (2021). Human Nasal and Lung Tissues Infected Ex Vivo with SARS-CoV-2 Provide Insights into Differential Tissue-Specific and Virus-Specific Innate Immune Responses in the Upper and Lower Respiratory Tract. J Virol *95*, e0013021. 10.1128/JVI.00130-21.
36. Chong, Z., Karl, C.E., Halfmann, P.J., Kawaoka, Y., Winkler, E.S., Keeler, S.P., Holtzman, M.J., Yu, J., and Diamond, M.S. (2022). Nasally delivered interferon-lambda protects mice against infection by SARS-CoV-2 variants including Omicron. Cell Rep *39*, 110799. 10.1016/j.celrep.2022.110799.
37. Robbiani, D.F., Gaebler, C., Muecksch, F., Lorenzi, J.C.C., Wang, Z., Cho, A., Agudelo, M., Barnes, C.O., Gazumyan, A., Finkin, S., et al. (2020). Convergent antibody responses to SARS-CoV-2 in convalescent individuals. Nature *584*, 437-442. 10.1038/s41586-020-2456-9.
38. Brouwer, P.J.M., Caniels, T.G., van der Straten, K., Snitselaar, J.L., Aldon, Y., Bangaru, S., Torres, J.L., Okba, N.M.A., Claireaux, M., Kerster, G., et al. (2020). Potent neutralizing antibodies from COVID-19 patients define multiple targets of vulnerability. Science *369*, 643-650. 10.1126/science.abc5902.
39. Kosik, I., Santos, J.D.S., Angel, M., Hu, Z., Holly, J., Gibbs, J.S., Gill, T., Kosikova, M., Li, T., Bakhache, W., et al. (2023). C1q Enables Influenza HA Stem Binding Antibodies to Block Viral Attachment and Broadens the Antibody Escape Repertoire. bioRxiv, 2023.2006.2012.544648. 10.1101/2023.06.12.544648.
40. Suzuki, R., Yamasoba, D., Kimura, I., Wang, L., Kishimoto, M., Ito, J., Morioka, Y., Nao, N., Nasser, H., Uriu, K., et al. (2022). Attenuated fusogenicity and pathogenicity of SARS-CoV-2 Omicron variant. Nature *603*, 700-705. 10.1038/s41586-022-04462-1.
41. Rajah, M.M., Hubert, M., Bishop, E., Saunders, N., Robinot, R., Grzelak, L., Planas, D., Dufloo, J., Gellenoncourt, S., Bongers, A., et al. (2021). SARS-CoV-2 Alpha, Beta, and Delta variants display enhanced Spike-mediated syncytia formation. EMBO J *40*, e108944. 10.15252/embj.2021108944.
42. Chang, C.W., Parsi, K.M., Somasundaran, M., Vanderleeden, E., Liu, P., Cruz, J., Cousineau, A., Finberg, R.W., and Kurt-Jones, E.A. (2022). A Newly Engineered A549 Cell Line Expressing ACE2 and TMPRSS2 Is Highly Permissive to SARS-CoV-2, Including the Delta and Omicron Variants. Viruses *14*. 10.3390/v14071369.
43. Lamers, M.M., Mykytyn, A.Z., Breugem, T.I., Wang, Y., Wu, D.C., Riesebosch, S., van den Doel, P.B., Schipper, D., Bestebroer, T., Wu, N.C., and Haagmans, B.L. (2021). Human airway cells prevent SARS-CoV-2 multibasic cleavage site cell culture adaptation. Elife *10*. 10.7554/eLife.66815.
44. Hill, V., Du Plessis, L., Peacock, T.P., Aggarwal, D., Colquhoun, R., Carabelli, A.M., Ellaby, N., Gallagher, E., Groves, N., Jackson, B., et al. (2022). The origins and molecular evolution of SARS-CoV-2 lineage B.1.1.7 in the UK. Virus Evol *8*, veac080. 10.1093/ve/veac080.
45. Kemp, S.A., Collier, D.A., Datir, R.P., Ferreira, I., Gayed, S., Jahun, A., Hosmillo, M., Rees-Spear, C., Mlcochova, P., Lumb, I.U., et al. (2021). SARS-CoV-2

evolution during treatment of chronic infection. Nature *592*, 277-282. 10.1038/s41586-021-03291-y.

46. Cele, S., Karim, F., Lustig, G., San, J.E., Hermanus, T., Tegally, H., Snyman, J., Moyo-Gwete, T., Wilkinson, E., Bernstein, M., et al. (2022). SARS-CoV-2 prolonged infection during advanced HIV disease evolves extensive immune escape. Cell Host Microbe *30*, 154-162 e155. 10.1016/j.chom.2022.01.005.
47. Choi, B., Choudhary, M.C., Regan, J., Sparks, J.A., Padera, R.F., Qiu, X., Solomon, I.H., Kuo, H.H., Boucau, J., Bowman, K., et al. (2020). Persistence and Evolution of SARS-CoV-2 in an Immunocompromised Host. N Engl J Med *383*, 2291-2293. 10.1056/NEJMc2031364.
48. Kupferschmidt, K. (2021). Where did 'weird' Omicron come from? Science *374*, 1179. 10.1126/science.acx9738.
49. Chaguza, C., Hahn, A.M., Petrone, M.E., Zhou, S., Ferguson, D., Breban, M.I., Pham, K., Pena-Hernandez, M.A., Castaldi, C., Hill, V., et al. (2023). Accelerated SARS-CoV-2 intrahost evolution leading to distinct genotypes during chronic infection. Cell Rep Med *4*, 100943. 10.1016/j.xcrm.2023.100943.
50. Corey, L., Beyrer, C., Cohen, M.S., Michael, N.L., Bedford, T., and Rolland, M. (2021). SARS-CoV-2 Variants in Patients with Immunosuppression. N Engl J Med *385*, 562-566. 10.1056/NEJMsb2104756.
51. Tamura, T., Yamasoba, D., Oda, Y., Ito, J., Kamasaki, T., Nao, N., Hashimoto, R., Fujioka, Y., Suzuki, R., Wang, L., et al. (2023). Comparative pathogenicity of SARS-CoV-2 Omicron subvariants including BA.1, BA.2, and BA.5. Commun Biol *6*, 772. 10.1038/s42003-023-05081-w.
52. Saito, A., Tamura, T., Zahradnik, J., Deguchi, S., Tabata, K., Anraku, Y., Kimura, I., Ito, J., Yamasoba, D., Nasser, H., et al. (2022). Virological characteristics of the SARS-CoV-2 Omicron BA.2.75 variant. Cell Host Microbe *30*, 1540-1555 e1515. 10.1016/j.chom.2022.10.003.
53. Yamasoba, D., Kimura, I., Nasser, H., Morioka, Y., Nao, N., Ito, J., Uriu, K., Tsuda, M., Zahradnik, J., Shirakawa, K., et al. (2022). Virological characteristics of the SARS-CoV-2 Omicron BA.2 spike. Cell *185*, 2103-2115 e2119. 10.1016/j.cell.2022.04.035.
54. Kimura, I., Yamasoba, D., Tamura, T., Nao, N., Suzuki, T., Oda, Y., Mitoma, S., Ito, J., Nasser, H., Zahradnik, J., et al. (2022). Virological characteristics of the SARS-CoV-2 Omicron BA.2 subvariants, including BA.4 and BA.5. Cell *185*, 3992-4007 e3916. 10.1016/j.cell.2022.09.018.
55. Kowarz, E., Loscher, D., and Marschalek, R. (2015). Optimized Sleeping Beauty transposons rapidly generate stable transgenic cell lines. Biotechnol J *10*, 647-653. 10.1002/biot.201400821.
56. Ye, C., Chiem, K., Park, J.G., Oladunni, F., Platt, R.N., 2nd, Anderson, T., Almazan, F., de la Torre, J.C., and Martinez-Sobrido, L. (2020). Rescue of SARS-CoV-2 from a Single Bacterial Artificial Chromosome. mBio *11*. 10.1128/mBio.02168-20.
57. Lawson, N.D., Stillman, E.A., Whitt, M.A., and Rose, J.K. (1995). Recombinant vesicular stomatitis viruses from DNA. Proc Natl Acad Sci U S A *92*, 4477-4481. 10.1073/pnas.92.10.4477.
58. Avanzato, V.A., Matson, M.J., Seifert, S.N., Pryce, R., Williamson, B.N., Anzick, S.L., Barbian, K., Judson, S.D., Fischer, E.R., Martens, C., et al. (2020). Case

Study: Prolonged Infectious SARS-CoV-2 Shedding from an Asymptomatic Immunocompromised Individual with Cancer. Cell *183*, 1901-1912 e1909. 10.1016/j.cell.2020.10.049.

59. Robinson, J.T., Thorvaldsdottir, H., Winckler, W., Guttman, M., Lander, E.S., Getz, G., and Mesirov, J.P. (2011). Integrative genomics viewer. Nat Biotechnol *29*, 24-26. 10.1038/nbt.1754.

60. Radvak, P., Kwon, H.J., Kosikova, M., Ortega-Rodriguez, U., Xiang, R., Phue, J.N., Shen, R.F., Rozzelle, J., Kapoor, N., Rabara, T., et al. (2021). SARS-CoV-2 B.1.1.7 (alpha) and B.1.351 (beta) variants induce pathogenic patterns in K18-hACE2 transgenic mice distinct from early strains. Nat Commun *12*, 6559. 10.1038/s41467-021-26803-w.

61. Kwon, H.J., Kosikova, M., Tang, W., Ortega-Rodriguez, U., Radvak, P., Xiang, R., Mercer, K.E., Muskhelishvili, L., Davis, K., Ward, J.M., et al. (2022). Enhanced virulence and waning vaccine-elicited antibodies account for breakthrough infections caused by SARS-CoV-2 delta and beyond. iScience *25*, 105507. 10.1016/j.isci.2022.105507.

62. Kwon, H.J., Zhang, J., Kosikova, M., Tang, W., Ortega-Rodriguez, U., Peng, H., Meseda, C.A., Pedro, C.L., Schmeisser, F., Lu, J., et al. (2023). Distinct in vitro and in vivo neutralization profiles of monoclonal antibodies elicited by the receptor binding domain of the ancestral SARS-CoV-2. J Med Virol *95*, e28673. 10.1002/jmv.28673.

63. Zhang, J., Tang, W., Gao, H., Lavine, C.L., Shi, W., Peng, H., Zhu, H., Anand, K., Kosikova, M., Kwon, H.J., et al. (2023). Structural and functional characteristics of the SARS-CoV-2 Omicron subvariant BA.2 spike protein. Nat Struct Mol Biol *30*, 980-990. 10.1038/s41594-023-01023-6.

Methods

Cell culture

We used baby hamster kidney fibroblast BHK21 (ATCC; CCL-10), African green monkey kidney Vero E6 (ATCC; C1008, Clone E6) Vero (provided by Dr. Nihal Altan-Bonnet, NHLBI), human embryonic kidney HEK293FT cells (Thermo Fisher; R70007), human lung adenocarcinoma A549 cells (ATCC; CCL-185) Calu-3 cells (ATCC; HTB-55), human colorectal adenocarcinoma Caco-2 cells (ATCC; HTB-37) cells. All cells were cultured in Dulbecco's modified Eagle's medium (DMEM) (Gibco; 10569044) supplemented with 10% fetal bovine serum (FBS, HyClone, no. SH30071.03) and 50 µg/ml Gentamicin (Quality Biological). We generated BHK21 cells stably expressing human ACE2 (BHK21-ACE2), A549 cells stably expressing human ACE2 (A549-ACE2), Vero E6 cells stably expressing human TMPRSS2 (Vero E6-TMPRSS2) and 293FT cells stably expressing T7 polymerase and VSVG (293FT-VSVG-T7pol) using the Sleeping Beauty transposon plasmid expression system [55]. Vero E6 cells stably expressing human ACE2 and TMPRSS2 (Vero E6-AT2) were obtained from BEI (NR-54970). A549 cells stably expressing human ACE2 and TMPRSS2 (ACE2plusC3, ATCC; CRL-3560) were provided by Dr. Ching-Wen Chang (University of Massachusetts Chan Medical School). Cell lines were confirmed to be mycoplasma-free using MycoStrip (InvivoGen, rep-mys-50). Primary human small airway epithelial cells (HSAEC, ATCC, PCS-301-010) were purchased from ATCC and maintained in PneumaCult™-Ex Plus Medium (STEMCELL Technologies) according to the manufacturer's instructions. All cell lines were incubated at 37 °C and 5% CO_2 in a humidified incubator.

Plasmid construction

The plasmid-based VSV reverse genetic system (pVSV eGFP dG) was obtained from Addgene (#31842) and modified to insert the wild-type S gene of the original Wuhan-Hu-1 strain of SARS-CoV-2 (GenBank MN908947.3) with a 21 amino acid deletion in its C terminal, between M and L genes, using standard molecular techniques. In brief, the VSV antigenome without the G gene and the SARS-CoV-2 S gene were amplified by PCR using Platinum™ SuperFi II PCR Master Mix (Thermo Fisher). PCR products were gel-purified and assembled using NEBuilder® HiFi DNA Assembly Master Mix (NEB). The assembled product was transformed into NEB 5-alpha Competent E. coli (NEB) using the standard protocol, and the cells were plated on carbenicillin LB agar plates (Quality Biological). Colonies were selected for Sanger sequencing to confirm the S gene insertion. Confirmed clones were cultured, and plasmids were isolated using the Midi prep plus kit (Qiagen).

pVSV-SARS-CoV-2-S with mCherry was constructed using the same method by replacing eGFP in the antigenome.

We generated rSARS-CoV-2 viruses using the bacterial artificial chromosome (BAC)-based SARS-CoV-2 reverse genetic system[56]. The pBAC-SARS-CoV-2-mCherry-2A was digested with BstBI (FastDigest, Thermo Fisher) and BamHI (FastDigest, Thermo Fisher) and the larger fragment was purified by Zymoclean Large Fragment DNA Recovery Kit (Zymo Research). An intermediate plasmid, pUC57-orf1-S, containing a portion of the pBAC-SARS-CoV-2 genome, was used to introduce mutations in the FCS of the S gene or to generate Delta- and Omicron-S variants. To generate pUC57-orf1-S R685S, P681R, site-directed mutagenesis was performed on the pUC57-orf1-S plasmid. To create pUC57-orf1-S Delta-S and Omicron-S, the WA1 S gene was replaced by the Delta or Omicron S gene using NEBuilder® HiFi DNA Assembly Master Mix following the manufacturer's instructions. Expected nucleotide sequences of pUC57-orf1-S with R685S, P681R, Delta or Omicron S gene were confirmed by Sanger sequencing. PCR reactions were conducted to amplify the fragment with partial orf1 and S genes, and products were assembled with the larger fragment by NEBuilder® HiFi DNA Assembly Master Mix. The assembled reaction was transformed into NEB® 10-beta Competent E. coli cells (NEB) following the manufacturer's instruction. Bacterial colonies were selected for Sanger sequencing to confirm the S gene sequence, and confirmed colonies were subjected to maxiprep to isolate the BCA plasmids.

The sleeping beauty system[55] was obtained from Addgene. Briefly, the genes for hACE2, TMPRSS2, codon-optimized T7 polymerase or VSVG were PCR amplified using primers containing BstBI restriction enzyme site. PCR products were purified and subcloned into pSBbi or tet-on inducible pSBtet vector that had been digested by BstBI. Confirmatory sequencing was performed on all constructs.

To express S we used a pHAGE-eGFP backbone vector. Briefly, genes encoding S and S variants were PCR amplified and subcloned into pHAGE-eGFP, forming an expression cassette of eGFP-IRES-S using NEBuilder® HiFi DNA Assembly Master Mix. All S genes lacked codons for the 21 C-terminal residues to increase cell surface expression. Codon-optimized full-length S-bearing pCAGGS plasmids, except the one containing *wt* S, were obtained as a gift from Marceline Côté at Addgene. wt S was generated by standard site mutagenesis from D614G S. All plasmids were sequenced to confirm nucleotide sequence fidelity.

Generation of stable cell lines

Stable cell lines, except as indicated, were generated by the Sleeping Beauty transposase system. Briefly, cells were seeded on a 60-mm plate, and the following day, cells were co-transfected with 0.5 µg of pCMV(CAT)T7-SB100 (transposase vector; Addgene, 34879) and 5 µg of pSBbi or pSBtet containing gene of interest using TransIT-LT1 transfection reagent (Mirus Bio), following the manufacturer's instructions. After 24 h, cells were detached and transferred to T-75 flasks, followed by selection with corresponding antibiotics for 2 weeks. Cell surface expression of hACE2 or TMPRSS2 was confirmed by flow cytometry. The functionality of T7 polymerase and VSVG expression in 293FT-T7pol-VSVG cell lines was determined using pUC19-T7pro-IRES-EGFP (Addgene, 138586) or through the recovery of rVSV virus.

Generation of rVSV-SARS-CoV-2 S

Due to the lower efficiency of the rVSV system for rescuing viruses[57], we optimized the rescue system using a stable 293FT cell line expressing T7 polymerase and VSVG, without using vaccina helper virus vTF7-3. This optimized system allowed us to efficiently recover rVSV-S, bearing an ancestral SARS-CoV-2 *wt* S as well as S variants. The generation of rVSV-S and its use in tissue culture at biosafety level 2 conditions was approved by the Institutional Biosafety Committee (IBC) at The National Institute of Allergy and Infectious Diseases (NIAID). Plasmid-based rescue of the rVSV was performed as described [28,29] with modifications. Briefly, 293FT-T7pol-VSVG cells in a 6-well plate were transfected with the VSV antigenome plasmid, along with plasmids expressing codon-optimized T7 polymerase (T7opt in pCAGGS, addgene, 65974), and VSV -N, -P, -L and -G-expressing plasmids (Addgene, 64087, 64088, 64085 and 8454), using TransIT-LT1 transfection reagent. Media were exchanged with fresh complete DMEM containing doxycycline (1ug/ml, for VSVG expression). Cells were monitored by fluorescence microscopy every day for 2-3 d. Transfected cells with GFP- or mCherry-positive clusters and typical cytopathic effect (CPE) were collected as passage 0 and inoculated into fresh BHK21-ACE2 cells to propagate viral stock P1, which underwent further propagations in BHK21-ACE2 cells. Viral passages were subjected to Sanger and next-generation sequencing to verify S gene or viral genome sequences. Plaque purification was performed on Vero cells with viral passage 4. Each purified plaque was Sanger sequenced for the entire S gene. Plaque-purified virus, along with rescued rVSV viruses bearing P681R, Delta, and Omicron S, were propagated in Vero E6-TMPRSS2 cells. Supernatants were confirmed by NGS, aliquoted, and stored at -80°C for further experiments.

Generation of recombinant SARS-CoV-2

Generating rSARS-CoV-2 viruses and their use in tissue culture at biosafety level 3 were approved by the Institutional Biosafety Committee (IBC) and the Dual Use Research of Concern Institutional

Review Entity (DURC-IRE) at NIAID. We fused the mCherry gene with the N gene via a 2A linker using a bacterial artificial chromosome-based SARS-CoV-2 reverse genetic system[56]. Confluent BHK21-ACE2 (2×10^6 cells/well in 6-well plates, duplicates) were transfected with 2.5 μg/well of pBAC-SARS-CoV-2 using TransIT-LT1 transfection reagent. Media were exchanged with fresh DMEM containing 2% FBS 6 h post-transfection. After 48-72 h, mCherry-positive cells displaying typical viral infection were detached and collected, along with supernatant, labeled as P0, and stored at −80°C. The P0 viral stock was centrifuged to remove cell debris and used to infect fresh Vero E6-TMPRSS2 cells for 48-72 h. The supernatant was collected as P1. After confirming the rescued virus (P1) by Sanger sequencing, the P0 virus underwent two rounds of propagation, resulting in a new virus stock (P2), which was titrated for further experiments after NGS confirmation of the viral genome sequence.

Virus infectivity titration

To titrate virus, Vero E6 or Vero E6-TMPRSS2 cells were seeded in a 12-well plate at 3×10^5 cells per well. The following day, viral stocks were serially diluted and inoculated onto confluent cells for 1 h with gentle shaking every 15 min. After removal of the inoculation, the cells were covered by 1× plaque MEM medium containing 4% FBS and 1.25% Avicel. At 24 h.p.i, cells were fixed with 4% paraformaldehyde (PFA) or 10% neutral buffered formalin (NBF) for 30 min at RT. The fixed plates were scanned using the high-content imaging system Cytation 5 (Agilent), with either the GFP channel for rVSV-S or the Texas red channel for rSARS-CoV-2 virus. Raw images were processed and stitched with Gen5 3.12 (Agilent) in a default setting, and focus-forming unit (FFU) was determined.

For titration of viral stocks collected from infected monolayer cells or ALI apical wash, Vero E6-TMPRSS2(for monolayer) or Vero E6-AT2 (for ALI Apical wash) cells were seeded in a black 96-well plate at 3×10^4 cells per well. The following day, viral supernatant was serially diluted and inoculated onto the cells for 1 h with gentle shaking every 15 min. After removal of the inoculation, fresh completed DMEM medium was added and incubated for 7-8 h. Following incubation, cells were fixed with 4% PFA or 10% NBF for 30 min at RT. The fixed plate was scanned by high-content imaging system Cytation 5 with either GFP channel for rVSV-S or Texas red channel for recombinant rSARS-CoV-2 virus. The raw images were processed and with Gen5 3.12 in a default setting, and FFU were determined using the cellular analysis mode. Alternatively, cells were detached by TrypLE™ Express Enzyme (Thermo Fisher), fixed by 4% PFA for 30 min at RT, and subjected to flow cytometry analysis.

RNA extraction, RT–PCR, and Sanger sequencing

Viral RNAs were extracted by the QIAamp Viral RNA Mini Kit (Qiagen) according to the manufacturer's instructions. After extraction, the RNAs were dissolved in 20 µl nuclease-free water. Two µl of RNA samples was used for reverse transcription with the AccuScript High-Fidelity 1st Strand cDNA Synthesis Kit (Agilent; 200820) using random hexamer primers. DNA fragments containing the entire S gene were amplified by PCR. The resulting DNAs were purified by the QIAquick PCR Purification Kit (Qiagen), and the sequences were determined by Sanger sequencing by Psomagen (Rockville, MD).

Next-generation sequencing

Ten µl viral stock total RNA was used as input for NGS library preparing following the Illumina Stranded Total RNA Prep, Ligation (Illumina). Purified libraries were quantified using the Kapa Library Quantification Kit (Roche), pooled in equimolar concentrations, and sequenced as 2 x 150 bp reads on the MiSeq instrument using the MiSeq Reagent Micro kit v2 (Illumina). Raw image files were converted to fastq files using bcl2fastq (v2.20.0.422, Illumina) and processed as previously described [58]. Reference sequences used for mapping included SARS-CoV-2 genome (MN985325.1), Delta and Omicron S sequences, as well as the rVSV-S construct sequence. Detected variants were confirmed by visual inspection using the Integrative Genomics Viewer[59].

Cultured Cell Infection

We infected Vero or ACE2plusC3 cells with rVSV-S or rSARS-CoV-2 as described [19]. In brief, cells were seeded in a 24-well plate one day prior to infection. on the following day, confluent cells were infected with rVSV-S or rSARS-CoV-2 at a MOI of 0.01 (or indicated MOI) at 37 °C for 1 h with gentle shaking at every 15 min. Cells were washed twice with DPBS and fresh complete medium was added. Supernatant was collected and centrifugated to remove cell debris and stored at -80 °C. Infected monolayers were fixed with 4% PFA for 30 min at RT and scanned by a Cytation 5 and fluorescence intensity was determined by cellular analysis mode in Gen5 3.12.

For time series measurement of replication kinetics (Fig. S3a-c), 100 FFU of each virus was applied to Vero cells in a 12-well plate. Images were captured at 24, 28, 36 and 48 h.p.i. Area and fluorescence intensity of infection foci were determined in cellular analysis mode in Gen5 3.12.

IFN-β inhibition of infection

Vero cells were pretreated with the indicated concentration of IFN-β (Peprotech; 300-02BC) for 18-20 h. Subsequently, cells were inoculated with either rVSV-S or rSARS-CoV-2 for 1 h. After

removing the inoculum, fresh media with the indicated concentration of IFN-β was added. Infected cells were either scanned live or after PFA fixation (4%) at indicated times. The fluorescence intensity of infection foci was determined using cellular analysis mode by Gen5 3.12.

For time series recording of rVSV-S infection in Vero cells under IFN-β treatment following the procedure described above cells were inoculated with WT and R685S at MOI 0.01 or indicated MOI for 1 h. Following inoculation, cells were washed, and fresh media with the corresponding concentration of IFN-β were added. At 18 h.p.i, plates were time-lapse recorded for eGFP channel using a 10× objective with Cytation 5 under 5% CO_2 at 37°C. The interval time was 30 min for the recording. The Video (supplementary video.1-4) was made by Gen5 3.12 by default setting.

Ruxolitinib treatment

A549-ACE2 cells were seeded in 24-well plate one day prior to infection. On the following day, the cells were treated with 2 μM ruxolitinib for 2 h and washed with PBS. Cells were then infected with *wt* or R685S virus with MOI of 0.05 for 1 h, washed, and fresh media with 2 μM ruxolitinib were added. Cells were then incubated for 48 or 72 h. The supernatant was centrifuged to remove cell debris and stored at -80°C. Infected monolayers were fixed by 4% PFA and scanned using a Cytation 5. Raw images were acquired, processed, and stitched with Gen5 3.12 by default settings. Cellular analysis mode was conducted to analyze the fluorescence intensity.

Competition assay

Competition assays were performed as described [19]. Ratios (50:50, 90:10, and 10:90 of *wt*: R685S) were determined by FFU derived from viral stocks. Cells were infected at an MOI of 0.1 (*wt* and R685S) as described in “Cultured Cell Infection” section. Infectivity titers were determined by flow cytometry as described above.

IFN-β viral infection inhibition

Vero cells were seeded in a black 96-well plate at a density of 3×10^4 cells per well and incubated overnight. Cells were treated with IFN-β at 4-fold serial dilutions for 20 h and infected with *wt* or R685S at an MOI of 0.05 for 1 h. Following inoculation, cells were washed, and fresh media were added to cells for incubation for 7 h at 37°C. Cells were then fixed with 4% PFA, and images were acquired using Cytation 5. Cellular analysis was performed to quantitate infections using Gen5 3.12. “Infection inhibition” was calculated by dividing the fluorescence intensity of IFN-β-treated samples by mock-treated samples.

Transfection-based cell-cell fusion assay

Vero cells were seeded in a 24-well plate at a density of 1.5×10^5 cells per well. The following day, receptor cells were transfected with pLifeAct-mScarlet. Donor cells were transfected with pHAGE-eGFP-IRES-S *wt* or R685S for 4-6 h and detached using trypLE. Detached donor cells were overlaid onto receptor cells at a 1:4 ratio for 20 h. Subsequently, cells were washed and fixed with 4% PFA. Images were acquired, and fluorescence intensity was determined as above.

Single-cycle influenza virus-based cell-cell fusion assay

Recombinant influenza PR8 virus with the HA gene was replaced by the mCherry gene, was used to infect donor Vero cells at an MOI of 0.02. Following inoculation, donor cells were transfected with an S-expression plasmid. Receptor Vero cells were transfected with the pmaxGFP plasmid for 20 h. Four h post-transfection, donor cells were detached and overlaid onto receptor cells at a 1:4 ratio for 24 h. Cells were washed with DPBS to remove floating cells before fixation with 4% PFA and imaging as above.

Fluorescent virus microneutralization assay

VN assays were conducted using rVSV-S or rSARS-CoV-2 virus, following previously established protocols[19]. Vero-ACE2 cells were plated on a black flat-bottom 96-well plate (Costar, 3603). The next day, mAbs were serially diluted in 4-fold dilutions and incubated with 500 FFU of rVSV-S *wt* or R685S expressing eGFP at 37°C for 30 min and the virus-antibody mixture was transferred to cells. After 7 h, the plate was sealed with a parafilm membrane and scanned for eGFP fluorescence on Cytation 5 under 5% CO_2 at 37°C. Subsequently, the plate was returned to the incubator at 5% CO_2 and 37°C. At 20 h.p.i, the plate was re-scanned for eGFP fluorescence using the same settings as at 7 h.p.i.

A similar experimental procedure was conducted for the neutralization assay for rSARS-CoV-2. Due to BSL-3 laboratory contamination, a duplicate plate of each infection was set in the rSARS-CoV-2 infection. Plates were fixed with 4% PFA for 30 min at 7 and 20 h.p.i, respectively.

Raw images (2 × 2 montage) for each well were acquired using a 4× objective, processed, and stitched using default settings. eGFP-positive or mCherry-positive objects were quantified for each well. VN activity was determined by dividing the eGFP or mCherry intensity of mAb treated cells by the intensity of correspond mock-treated cells. The nonlinear regression fit (dose-response model) was employed to determine the neutralization dose 50% of eGFP or mCherry fluorescence (ND_{50}).

IFN inhibition titration

Vero or ACE2plusC3 cells were seeded in a black flat-bottom 96-well plate (Costar, 3603). The following day, cells were treated with varying doses of recombinant human IFN-α2 (Sino Biological; 13833-HNAY), IFN-β (Peprotech; 300-02BC), IFN-γ (Peprotech; 300-02), or IFN-λ2 (Peprotech; 300-02K) for 18-20 h before infection. Media were replaced with viral infection medium the next day, and fresh media containing IFN was added after 1 h inoculation. Cells were fixed with 4% PFA at RT for 30 min 20- or 24-h post-infection. Raw images of infected monolayers were acquired using Cytation 5. IFN inhibitions was calculated by ratio of fluorescence intensity of infection with IFN *vs.* mock treatment.

Fusion Index calculation

For calculating the fusion index in rVSV-S infection in Vero cells, infected and non-infected (mock infected) cells were permeabilized and counterstained with DAPI for 10 min at RT. Raw montages (3×8=24) of infected cells were captured in DAPI and GFP channels using the high-content imaging system Cytation 5 with a 20x objective. The aggregation of nuclei (as shown in Fig. 4a,e) in syncytia making it difficult to count the nuclei number in syncytia directly. To do that, we first counted DAPI stained nuclei in mock infected cells using Gen5 to determine the total number of cells which represents the total number of cells in infection ($N_{\text{cell total}}$). We determined the number of non-infected cells ($N_{\text{cell no-infection}}$) in infected wells by using a GFP background level determined from non-infected cultures. We determined the number of non-syncytial cells ($N_{\text{cell single}}$), including single infected and non-infected cells, based on the area of the DAPI signal (Gen5 setting: object size < 400 μm², the area of a single nucleus ranges from about 250-360 μm² *in situ*). The fusion index was then calculated using the following formula:

$$Fusion\ index = \frac{N_{cell\ total} - N_{cell\ single}}{N_{cell\ single} - N_{cell\ no-infection}}$$

Human respiratory epithelial cells in air-liquid interface format and infection

Human small airway epithelial cells were obtained from ATCC (PCS-301-010™, 3 donors: Lot Number: 70034740, 70035986, 70036650). After two passages in cell proliferation media (PneumaCult-Ex Plus medium, STEMCELL Technologies) supplemented with antibiotics, cells were seeded on Transwell inserts (0.4-micron pore size, 6.5mm, Corning; 3470) at a density of 33,000 cells per insert with media added to both the basal and apical sides. Once cells reached confluence, media were replaced with PneumaCult-ALI-S medium (STEMCELL Technologies) in the basal chamber, and the apical surface was exposed to establish an air-liquid interface (ALI). Monolayers were cultured at ALI for 4 weeks to promote differentiation into small airway

epithelium. Nasal epithelium ALI was purchased from Epithelix (Plan-les-Ouates, Switzerland), which was differentiated from pooled cells of 14 donors (Batch Number: MP0011, differentiated on February 17th,2023; Experiments were performed in June 2023.), and was maintained in MucilAir™ medium (Epithelix).

For SARS-CoV-2 infection, differentiated ALI cultures were pretreated on the basal side with human IFN-β or IFN-λ2 at 0.2 or 10 ng/ml, respectively, for 20-24 h. Control wells were mock-treated with PBS. Following treatment, the apical side of the ALI was washed twice with DPBS for 5 min at 37°C to remove mucus. Cells were then inoculated with rSARS-CoV-2 *wt* or R685S virus at 10^4 FFU diluted in 100 µl of plain DMEM at the apical side for 2 h at 37°C. After inoculation, the apical side was washed twice with DPBS and exposed to an air-liquid interface. The culture medium in the basal chamber was replaced with fresh IFN at 2 d.p.i, and 15 µl of fresh medium containing the corresponding IFN were added to the apical chamber to prevent drying after mucus removal, which would reduce cilia beating frequency. At 4 d.p.i., apical washes with DPBS for 20 min at 37°C were collected for further titration. Infected cells in the transwell were fixed with 4% PFA for 60 min before removal from the BSL-3 containment area.

Immunofluorescence staining

The following primary Abs and IF dilutions were used in this study: Rabbit polyclonal anti-SARS-CoV-2-N (GeneTex, GTX135357, 1:500), rabbit monoclonal Alexa Fluor® 647 conjugated anti-Cytokeratin 5 (Cytk5, Abcam, ab193895, 1:200), rabbit monoclonal anti-Acetyl-α-tubulin (AcTub, Cell Signaling, 5335, 1:1000), mouse monoclonal Ab anti-Mucin 5AC (Muc5A, Invitrogen, MA5-12178, 1:100). The following secondary Abs were used in this study: cross-absorbed Goat anti-rabbit Alexa Fluor 750 or 488 (Invitrogen, A21039/A11008, 1:1000), cross-absorbed Goat anti-mouse Alexa Fluor 488 (Invitrogen, A11029, 1:1000).

For antigen detection, rSARS-CoV-2 infected epithelia were washed in DPBS and permeabilized with 0.5% TritonX-100 in DPBS for 20 min at RT and blocked with IF buffer (DPBS containing 5% normal Goat serum and 0.1% TritonX-100) for 1 h at RT after extensive washing with DPBS. Primary Abs were diluted in antibody dilution buffer (DPBS containing 1% BSA and 0.1% TritonX-100) and applied to inserts for 1 h at RT or overnight at 4°C. After three washes with DPBS, samples were incubated with secondary Abs for 1 h at RT. In the case of the primary antibody (Anti-Cytk5-AF647) derived from the same species as anti-AcTub, sequential staining was performed. Samples were incubated with 2 µg/ml of DAPI for 10 min at RT. Inserts were then washed extensively in DPBS, and membranes were removed from inserts and mounted in VECTASHIELD® Antifade Mounting Media (Vector Laboratories) prior to microscopy analysis.

Microscopy and image analysis

For full ALI epithelial overviews, high-content imaging was performed using the Cytation 5 system with a 4X objective in a 24-well black glass bottom plate (Cellvis). Raw images were processed and stitched by default settings. Cellular analysis mode with object size ranging from 5 to 1000 μm was performed to quantify the overall fluorescence intensity of infection by Gen 5 3.12.

Ab stained infection foci were imaged using a Leica Stellaris 8 (Leica Microsystems, no. 11513859) in Z-stack mode, and three-dimensional (3D) reconstructions were done with Imaris in 3D view mode. The entire epithelia were tile scanned using a 63X 1.4 oil objective in low resolution with the LAS-X Navigator function. This entailed scanning 40x40 fields at 512x512 pixel resolution (1600 fields in total) for the mCherry channel. Subsequently, 20-45 random fields of infection were selected for Z-stack scanning, covering five channels (DAPI for nuclei, Alexa Fluor 488 for Muc5A, mCherry for rSARS-CoV-2 infection, Alexa Fluor 647 for Cytk5, and Alexa Fluor 750 for AcTub) for each epithelium. Images were captured at 1024 x 1024 pixel resolution with a step size of 0.25 μm. Representative images were processed by LAS-X software or Imaris (Bitplane).

To quantify syncytia (nuclei), randomly acquired fields were reconstructed into 3D structures, and individual planes were analyzed with Leica LAS-X software. The mCherry signal was used as a marker of infected cells, and the number of nuclei within each infected focus was determined by eye.

Mouse infection

B6.Cg-Tg(K18-ACE2)2Prlmn/J (K18) transgenic mice (JAX Stock No. 034860) were bred at FDA White Oak Vivarium. Homozygous K18 mice of both sexes at approximately 8−12 weeks were inoculated with rSARS-CoV-2 *wt* or R685S at 2000 FFU/50 μl/mouse under light isoflurane anesthesia. One day before and one day post infection, mice were treated i.n. with recombinant murine IFN-λ2 (Peprotech cat no. 250-33) at 2 μg/50 μl/mouse or 50 μl/mouse of PBS (mock-treated). Three d.p.i, mice were euthanized, and whole lungs were harvested for viral infectivity/PCR titers and cytokine determination. Procedures were performed according to the animal study protocols approved by the FDA White Oak Animal Program Animal Care and Use Committee.

Determination of lung viral titers

Lung viral titers were measured using both real-time PCR [60-62] and focus-forming assay (FFA) [63]. RNA was extracted from whole lung homogenates using RNeasy Plus Mini Kit (Qiagen #74136)

and converted to cDNA using the High-Capacity cDNA Reverse Transcription Kit (Thermo Fisher Scientific #4368813). Copy numbers of SARS-CoV-2 nucleocapsid (N) gene in lung tissues were determined using 2019-nCoV RUO Kit (Integrated DNA Technologies #10006713 and QuantiNova SYBR Green PCR kit (Qiagen #208052) according to the following cycling program: 95°C for 120 s, 95°C for 5 s (50 cycles), and 60°C for 18 s [60-62]. Results were calculated based on a standard curve constructed using threshold cycle (Ct) values of serially diluted pCC1-CoV2-F7 plasmid expressing SARS-CoV-2 N. A value of 1 was assigned if gene copies were below the detection limits. FFA was also conducted to measure infectious viral particles in lung homogenates[63]. Supernatants of lung homogenates were serially diluted in MEM with 2% FBS and 1% antibiotics and were added to Vero E6 with human TMPRRS2 overexpression (BPS Bioscience #78081) pre-seeded in 96-well tissue culture plates. Following the incubation at 37 °C and 5% CO_2 for 1 h, unattached viruses were removed, and cells were overlaid with 1.2% Avicel (DuPont) after 1:1 (v/v) mixing with 2x EMEM with 4% FBS and 2% antibiotics [63]. Cells were incubated at 37 °C and 5% CO_2 for up to 24 h. After fixing and permeabilization, viral foci were detected using anti-nucleocapsid rabbit mAb (1:6,000; Sino Biological #40143-R001) and bound Ab detected by peroxidase-conjugated goat anti-rabbit secondary antibody (1:2,000; SeraCare #5220-0336) followed by KPL TrueBlue substrate (SeraCare #5510-0030) [63].

Multiplex proinflammatory cytokine measurement

Proinflammatory cytokines in mouse lung homogenates were measured using a V-PLEX Proinflammatory Panel 1 Mouse Kit (Meso Scale Discovery # K15048D) according to the manufacturer's instructions. Data were acquired in a MESO QuickPlex SQ 120 imager equipped with MSD Discovery Workbench 4.0.12 (LSR_4_0_12).

Cell-cell fusion assay

One T75 flask of Vero cells was transfected with a DSP_{1-7} expression plasmid while another T75 Vero cells was transfected with a DSP_{8-11} expression plasmid. Four h post-transfection cells were detached using TrypLE and mixed at 1:1 ratio and in 24-well plates. The following day, mixed cells were transfected with pCAGGS-SARS-CoV-2 S plasmids expressing codon-optimized full-length S or S variants. 24 h post-transfection, cells were washed and fixed by 4% PFA for 20 min at RT before being subjected to high-content imaging.

For cell-cell fusion in 293FT and Clau-3 cells, 293FT cells were co-transfected with pmaxGFP and pCAGGS-SARS-CoV-2 S plasmids. Control samples were co-transfected with pmaxGFP and pCAGGS empty plasmids. Four h post-transfection, 293FT cells were detached and overlayed

onto 100% confluent Calu-3 cells at a ratio of 1: 50. After 24 h, cells were washed and fixed with 4% PFA for 20 min at RT before being subjected to high-content imaging. Raw images were processed and stitched by default settings. Cellular analysis mode was performed to determine the overall fluorescence intensity and area of GFP-positive foci.

Sequence Alignment and phylogenetic tree

S sequence alignment and phylogenetic tree were generated by using full-length S protein sequence with Clustal Omega. Sequences were acquired from NCBI with accession numbers: OC43-CoV, AXX83381.1; MERS-CoV, YP_009047204.1; SARS-CoV, YP_009825051.1; SARS-CoV-2, YP_009724390.1; Bat-RatG13, QHR63300.2.

Statistical analysis

All statistical tests were performed as described in the figure legends using Prism v9(GraphPad Software, Inc.). The number of independent experiments performed is indicated in the relevant figure legends. Statistical significance is set as $P < 0.05$, and P values are indicated with: NS, not significant; *$P < 0.05$; **$P < 0.01$; ***$P < 0.001$, ****$P < 0.0001$.

Data availability

All data supporting the conclusions of this study are reported in the paper. The raw data are available from the corresponding author upon reasonable request. Source data are provided in this paper.

Figure S1 Furin cleavage site(FCS) motif in SARS-CoV-2 dominant circulating variants.

Alignment of the region of S gene containing FCS motif from SARS-CoV-2 dominant circulating variants in an order of emergency in time. The RXXR furin cleavage motif (682-685 in Wuhan-Hu-1) is marked in a black rectangle. The proximal residue at 681 which affects the cleavage efficiency and syncytia is indicated in arrowhead. The hallmark mutation at 681 in Delta and the new emerging Omicron subvariant BA.2.86 are marked in blue; other Omicron subvariants except BA.2.86 are marked in red. Sequences were acquired from NCBI with access number being: YP_009724390.1, QQH18533.1, WLL57934.1, UVN17823.1, UFT00449.1, UIG03312.1, USV68346.1, WMV91511.1, WKR02063.1, UPU09668.1, UWM38596.1, UYH63216.1, BES80299.1, BES80198.1, WGP26425.1, WLW39834.1 . Alignment was generated by ClustalOmega using full-length S protein sequence.

Figure S2 Generation of replication-competent chimeric SARS-CoV-2 S bearing VSV virus and forward genetic selection of fitness-advantaged mutants.

a Stable cell line 293FT cells expressing VSVG and T7 polymerase were transfected with plasmids VSV-N, -P, -L, -G, and codon-optimized T7 polymerase and an infectious molecular cDNA of pVSV-eGFP-SARS-CoV-2-S to produce replication-competent VSV-eGFP-SARS-CoV-2-S (referred as rVSV-S), the rescued viral stock (P0) was then passaged 4 times in BHK21 cells stably expressing human ACE2 (BHK21-ACE2).

b FCS mutations were identified by Sanger sequencing on passaged rVSV- S on the whole S gene. The region of FCS was shown to show double peaks at G2045 (R682 at amino acid level) in S gene in passages 3 to 5, but not in passage 2. Another mutation at G2054(R685 at amino level) was observed in P4 and P5.

c Titer of plaque-purified rVSV-S *wt* and mutants. Four mutants with mutations in FCS were identified in a plaque-purified assay, titer was measured in BHK21-ACE2 cells, and all FCS mutants gained growth advantage in BHK21-ACE2 cells(n=3). Data show mean ± s.d.

d Competition assay between rVSV- S *wt* and R685S at total MOI of 0.01, showing infected cells by eGFP(R685S) and mCherry (*wt*) channels. The input ratio was for inoculation, and the output infection percentage was detected by flow cytometry at 7 h.p.i (n=3). Data show mean ± s.d.

Figure S3 FCS mutant R685S gains fitness advantage in Vero cell.

a Time-lapse image of rVSV-S *wt* and R685S infections in Vero cell, with 100 FFU/well in a 12-well plate in inoculation.

b and **c** Replication dynamics of rVSV-S *wt* and R685S infections in Vero cells. Mean fluorescence intensity (MFI) of each infectious focus was measured(**b**). Data show mean ± s.d. (**b**, n=4). Focus area was compared between rVSV-S *wt* and R685S at 24 h.p.i(left) and 28 h.p.i(right)(**c**), n= 152 and 96 for *wt* and R685S, respectively. Data show the geometric mean ± 95% CI (**c**).

d Infection of recombinant rSARS-CoV-2 *wt* (WA-1 strain) and R685S mutant, with expression of mCherry gene linked to nucleoprotein via a 2A linker, in Vero cells at 36 h.p.i in a 12-well plate. Two representative images for each virus (rep1 and rep2) were shown. Cells were overlayed with 1.25% avicel after infection.

e Mean fluorescence intensity of infection foci as shown in **d** (n=3). Data show mean ± s.d.

f Individual area of infection foci as shown in d, n= 48 and 82 for *wt* and R685S, respectively. Data show the geometric mean ± 95% CI. Each dot represents one focus in **c** and **f**. For **c** and **f**, statistical analysis was performed using a two-sided, unpaired Mann-Whitney test. *P < 0.05, **P < 0.01, ***P < 0.001 and ****P < 0.0001; NS, not significant. The data show representative of two independent experiments.

Figure S4 Sensitivity of *wt* and R685S to IFN-β in Vero cells in VSV system.

a Representative images of rVSV-S *wt* and R685S infections under exogenous IFN-β treatment in Vero cells at 48 h.p.i, in 12-well plates. Cells were pretreated with IFN-β for 18-20 h prior to infection, and corresponding IFN was maintained throughout the infection.

b Fluorescence intensity of each infection with different MOI and various concentrations of IFN-β. Results are representative of two independent experiments.

Figure S5 Sensitivity of *wt* and R685S to IFN-β in Vero cells in SARS-CoV-2 system.

a Representative images of rSARS-CoV-2 *wt* and R685S infections under exogenous IFN-β (0.1 ng/ml) treatment in Vero cells at MOI of 0.01. Cells were pretreated with IFN-β for 18-20 h prior to infection, and corresponding IFN was maintained throughout the infection. Scale bar, 500 μm.

b Infection focus area of rSARS-CoV-2 *wt* and R685S under IFN-β treatment at the concentration of 0.05 (up) and 0.1 (bottom) ng/ml. Data show mean ± s.e.m. each dot represents one infection focus. Results are representative of three independent experiments. Statistical analysis was performed using a two-sided, unpaired Mann-Whitney test. ***P < 0.001 and ****P < 0.0001; ns, not significant.

Figure S6 Syncytia but not cell-free spread confers virus resistance to IFN-β anti-viral activity.

a Effects of IFN-β on rVSV-S *wt* fusion ratio in Vero cells. Pretreated Vero cells by IFN-β were infected by rVSV-S, cells were overlaid without(left) or with(right) agar for 24 h with IFN-β in the medium. Infected cells were fixed and scanned by the high-content imaging system Cytation 5. Fusion ratio (%) was calculated by dividing the infection area of syncytia by the total infected area. In Gen 5: the size of object was set to >60 μm to calculate the area of syncytia, which is about 3-fold the size of a single Vero cell *in situ* (n=3). Data show mean ± s.d.

b Representative images of rVSV- S R685S infection in Vero cells under IFN-b, linked to images in Fig.2h for comparison. BF means bright field, and Merge was conducted between BF and DAPI to show syncytia formation.

Data show mean ± s.d. Statistical analysis was performed using a one-way ANOVA(**a**) with multiple comparisons. ***P < 0.001 and ****P < 0.0001; ns, not significant. Results are representative of two independent experiments.

Figure S7 SARS-CoV-2 infection in human respiratory tract epithelial cells in air-liquid interface format.

a Cell types in syncytia formation, related to Fig. 3g. Infected small airway ALI were stained with anti-AcTub (green signal, marker for ciliated cell), anti-Cytk5 (yellow signal, marker for basal cell) and anti-Muc5A (cyan signal, marker for goblet cell) Abs and counterstained with DAPI (gray signal). Individual syncytia were shown from 3D reconstructed confocal images. Scale bar, 5μm.

b Entire Nasal epithelial cell ALI infected by rSARS-CoV-2 *wt* (left) and R685S mutant(right), related to Fig. 3h.

Figure S8 Proinflammation cytokine profile in lung tissue of K18-hACE2 mice infected by rSARS-CoV-2 *wt* and R685S mutant.

a Schematic workflow of rSARS-CoV-2 infection in K18 mice treated with murine IFN-λ2. I.N, Intranasal.

b Proinflammation cytokine expression level in lung tissues of infected K18 mice with or without IFN-λ2 treatment. Data show the combination of two independent experiments. Data show mean ± s.d (n=11). Statistical analysis was performed using two-way ANOVA (**b**). *P < 0.05, **P < 0.01, ***P < 0.001 and ****P < 0.0001; ns, not significant.

Figure S9 Monoclonal antibody neutralization profile against *wt* and R685S mutant infection.

A two-timepoints assay was performed to assess the contribution of syncytia spread of virus to the neutralization effect.

a and **b** Neutralization profile of 6 potent mAbs targeting RBD of S against rVSV-S *wt* and R685S infection in Vero-ACE2 cells. Representative images of rVSV-S *wt* and R685S infection at 20 h.p.i were shown (**a**, top left panel). Raw neutralization data were performed in nonlinear regression analysis (**a**, top right and bottom panel). 50% neutralization dose (ND_{50}) of each antibody was determined and shown (**b**).

c and **d** Neutralization profile of 6 potent mAbs against rSARS2 *wt* and R685S infection in ACE2plusC3 cells. Representative images of rSARS-CoV-2 *wt* and R685S infection at 20 h.p.i were shown (**c**, top left panel). The neutralization curve was fitted with nonlinear regression analysis, and the ND_{50} of each antibody was determined(**d**).

Data show mean ± s.d (n=3). Statistical analysis was performed using a two-sided Wilcoxon matched pair signed rank test. *P < 0.05; ns, not significant.

Figure S10 Syncytia mediated by S variants.

a Syncytia formation in Vero cells mediated by S-expressing plasmids, containing *wt*, P681R, P681H, Delta or Omicron (BA.1) S. Representative images at 20 h.p.i (left) and GFP positive area normalized to *wt* (right) was shown. Data show mean ± s.d (n=3). Scale bar, 100 μm.

b fusion index calculation workflow, fusion index was defined as described in the Method section. Scale bar, 100 μm.

c Syncytia formation in ACE2plusC3 cells mediated by rSARS-CoV-2 virus infection, containing *wt*, R685S, P681R, Delta or Omicron (BA.1) S. Representative images at 20 h.p.i were shown. Scale bar, 100 μm. Statistical analysis was performed using one-way ANOVA. *P < 0.05, **P < 0.01, ***P < 0.001 and ****P < 0.0001; ns, not significant.

Figure S11 Proportion of dominant SARS-CoV-2 variants over time.

Daily global reported infection case and vaccination datasets were downloaded from Our World in Data (https://ourworldindata.org/covid-vaccinations) as of July 2023. The dataset was plotted by Python program. The white line shows daily new confirmed COVID-19 cases in 7-day rolling average.

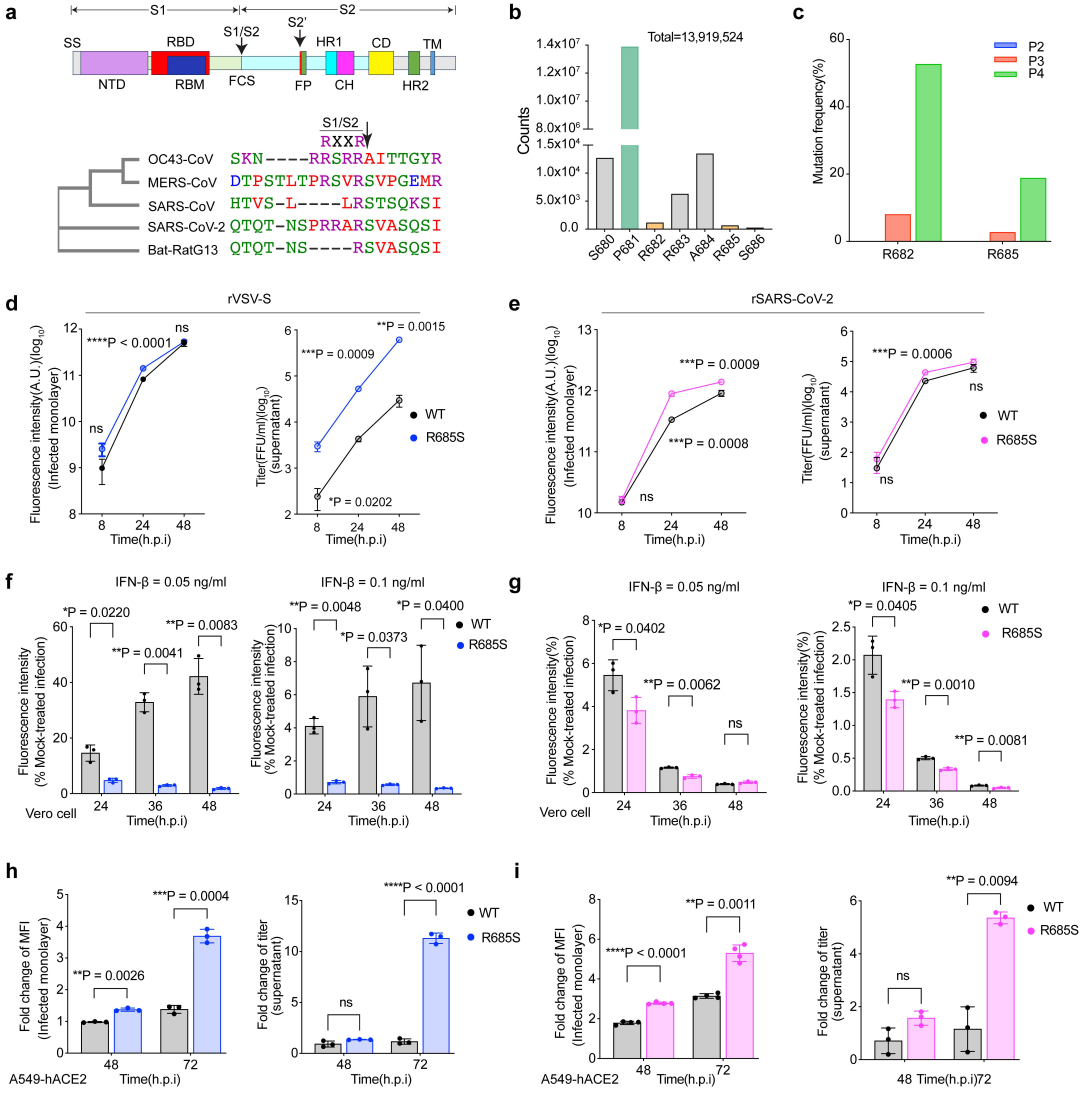
a
S1
S2
S2'
SS
RBD
S1/S2
HR1
CD
TM
NTD
RBM
FCS
FP
CH
HR2
S1/S2
RXXR
OC43-CoV SKN----RRSRRAITTGYR
MERS-CoV DTPSTLTPRSVRSVPGEMR
SARS-CoV HTVS-L----LRSTSQKSI
SARS-CoV-2 QTQT-NSPRRARSVASQSI
Bat-RatG13 QTQT-NS----RSVASQSI
b
Total=13,919,524
Counts
S680
P681
R682
R683
A684
R685
S686
c
Mutation frequency(%)
P2
P3
P4
R682
R685
d
rVSV-S
Fluorescence intensity(A.U.)(log10) (Infected monolayer)
****P < 0.0001
ns
ns
Time(h.p.i)
Titer(FFU/ml)(log10) (supernatant)
***P = 0.0009
**P = 0.0015
*P = 0.0202
WT
R685S
e
rSARS-CoV-2
***P = 0.0009
***P = 0.0008
ns
***P = 0.0006
ns
ns
f
IFN-β = 0.05 ng/ml
IFN-β = 0.1 ng/ml
Fluorescence intensity (% Mock-treated infection)
*P = 0.0220
**P = 0.0041
**P = 0.0083
**P = 0.0048
*P = 0.0373
*P = 0.0400
Vero cell
Time(h.p.i)
WT
R685S
g
IFN-β = 0.05 ng/ml
IFN-β = 0.1 ng/ml
Fluorescence intensity(%) (% Mock-treated infection)
*P = 0.0402
**P = 0.0062
ns
*P = 0.0405
**P = 0.0010
**P = 0.0081
Vero cell
Time(h.p.i)
WT
R685S
h
Fold change of MFI (Infected monolayer)
**P = 0.0026
***P = 0.0004
A549-hACE2
Time(h.p.i)
Fold change of titer (supernatant)
****P < 0.0001
ns
WT
R685S
i
Fold change of MFI (Infected monolayer)
****P < 0.0001
**P = 0.0011
A549-hACE2
Time(h.p.i)
Fold change of titer (supernatant)
**P = 0.0094
ns
WT
R685S
48 Time(h.p.i)72

Figure.1

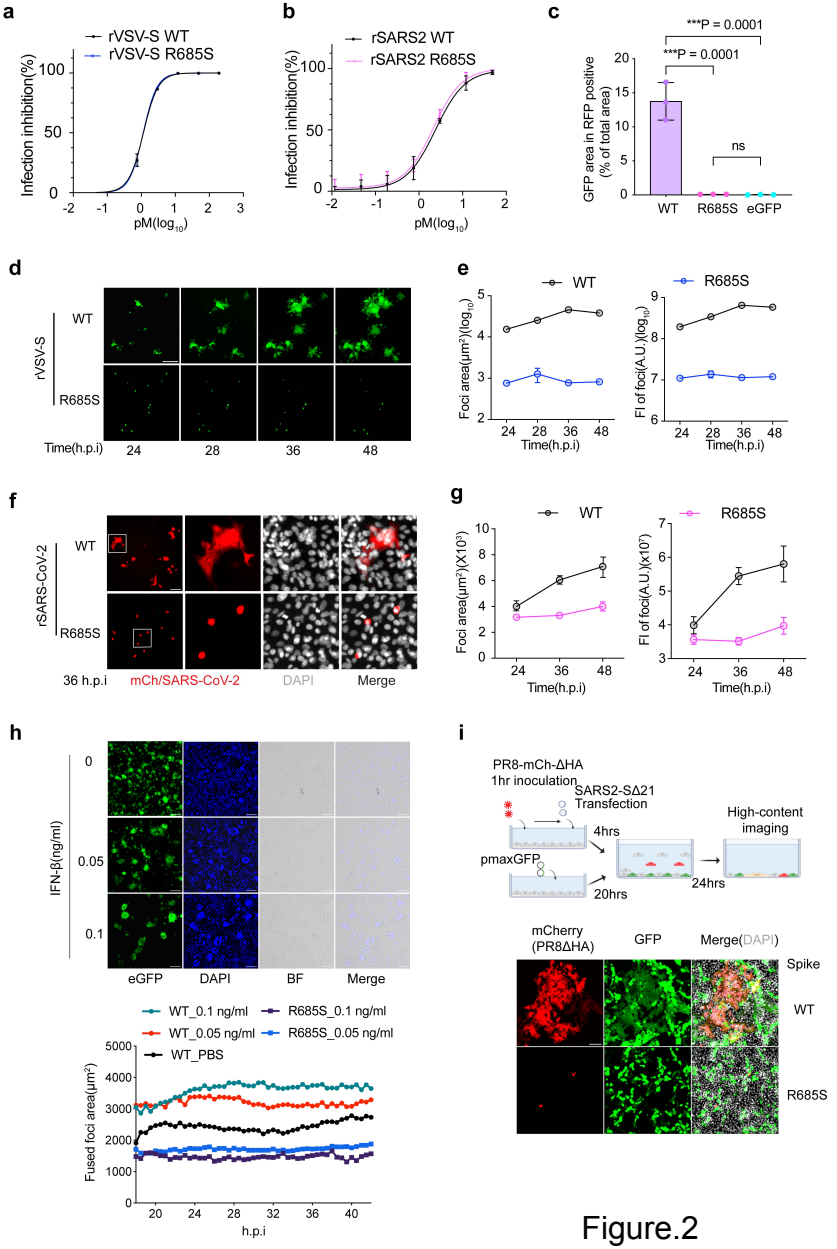
a
rVSV-S WT
rVSV-S R685S
Infection inhibition(%)
pM(log10)
b
rSARS2 WT
rSARS2 R685S
Infection inhibition(%)
pM(log10)
c
***P = 0.0001
***P = 0.0001
ns
GFP area in RFP positive (% of total area)
WT
R685S
eGFP
d
rVSV-S
WT
R685S
Time(h.p.i)
24
28
36
48
e
WT
R685S
Foci area(μm²)(log10)
FI of foci(A.U.)(log10)
Time(h.p.i)
f
rSARS-CoV-2
WT
R685S
36 h.p.i
mCh/SARS-CoV-2
DAPI
Merge
g
WT
R685S
Foci area(μm²)(X10³)
FI of foci(A.U.)(x10⁷)
Time(h.p.i)
h
IFN-β(ng/ml)
0
0.05
0.1
eGFP
DAPI
BF
Merge
WT_0.1 ng/ml
WT_0.05 ng/ml
WT_PBS
R685S_0.1 ng/ml
R685S_0.05 ng/ml
Fused foci area(μm²)
h.p.i
i
PR8-mCh-ΔHA
1hr inoculation
SARS2-SΔ21
Transfection
4hrs
pmaxGFP
20hrs
24hrs
High-content imaging
mCherry (PR8ΔHA)
GFP
Merge(DAPI)
Spike
WT
R685S

Figure.2

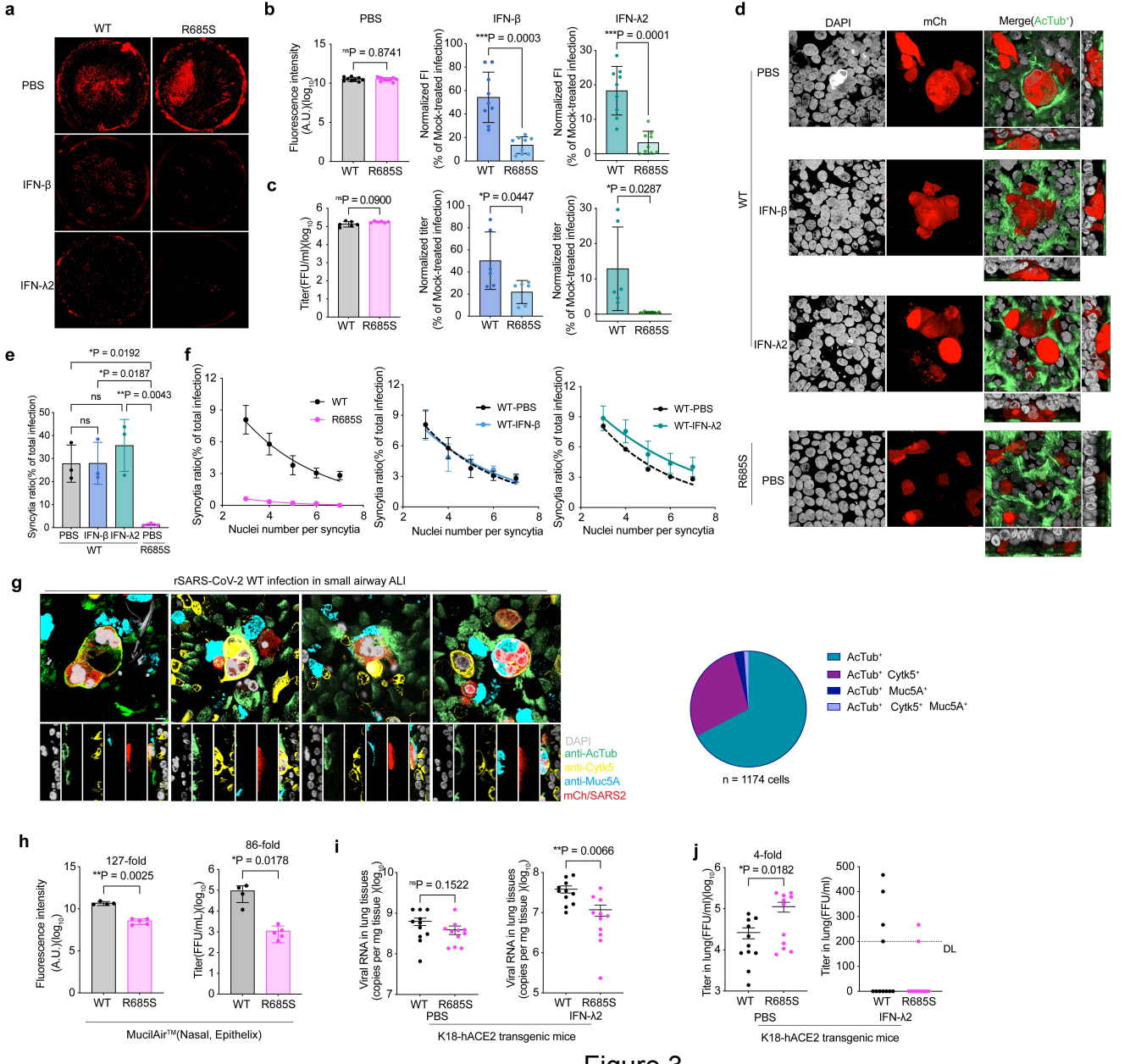
a
WT
R685S
PBS
IFN-β
IFN-λ2
b
PBS
IFN-β
IFN-λ2
Fluorescence intensity (A.U.)(log10)
nsP = 0.8741
***P = 0.0003
***P = 0.0001
Normalized FI (% of Mock-treated infection)
WT
R685S
c
nsP = 0.0900
*P = 0.0447
*P = 0.0287
Titer(FFU/ml)(log10)
Normalized titer (% of Mock-treated infection)
d
DAPI
mCh
Merge(AcTub+)
WT
R685S
PBS
IFN-β
IFN-λ2
e
*P = 0.0192
*P = 0.0187
ns
**P = 0.0043
Syncytia ratio(% of total infection)
PBS
IFN-β
IFN-λ2
f
WT
R685S
WT-PBS
WT-IFN-β
WT-IFN-λ2
Nuclei number per syncytia
g
rSARS-CoV-2 WT infection in small airway ALI
DAPI
anti-AcTub
anti-Cytk5
anti-Muc5A
mCh/SARS2
AcTub+
AcTub+ Cytk5+
AcTub+ Muc5A+
AcTub+ Cytk5+ Muc5A+
n = 1174 cells
h
127-fold
**P = 0.0025
86-fold
*P = 0.0178
Fluorescence intensity (A.U.)(log10)
Titer(FFU/mL)(log10)
MucilAir™(Nasal, Epithelix)
i
nsP = 0.1522
**P = 0.0066
Viral RNA in lung tissues (copies per mg tissue)(log10)
PBS
IFN-λ2
K18-hACE2 transgenic mice
j
4-fold
*P = 0.0182
Titer in lung(FFU/ml)(log10)
Titer in lung(FFU/ml)
DL
PBS
IFN-λ2
K18-hACE2 transgenic mice

Figure.3

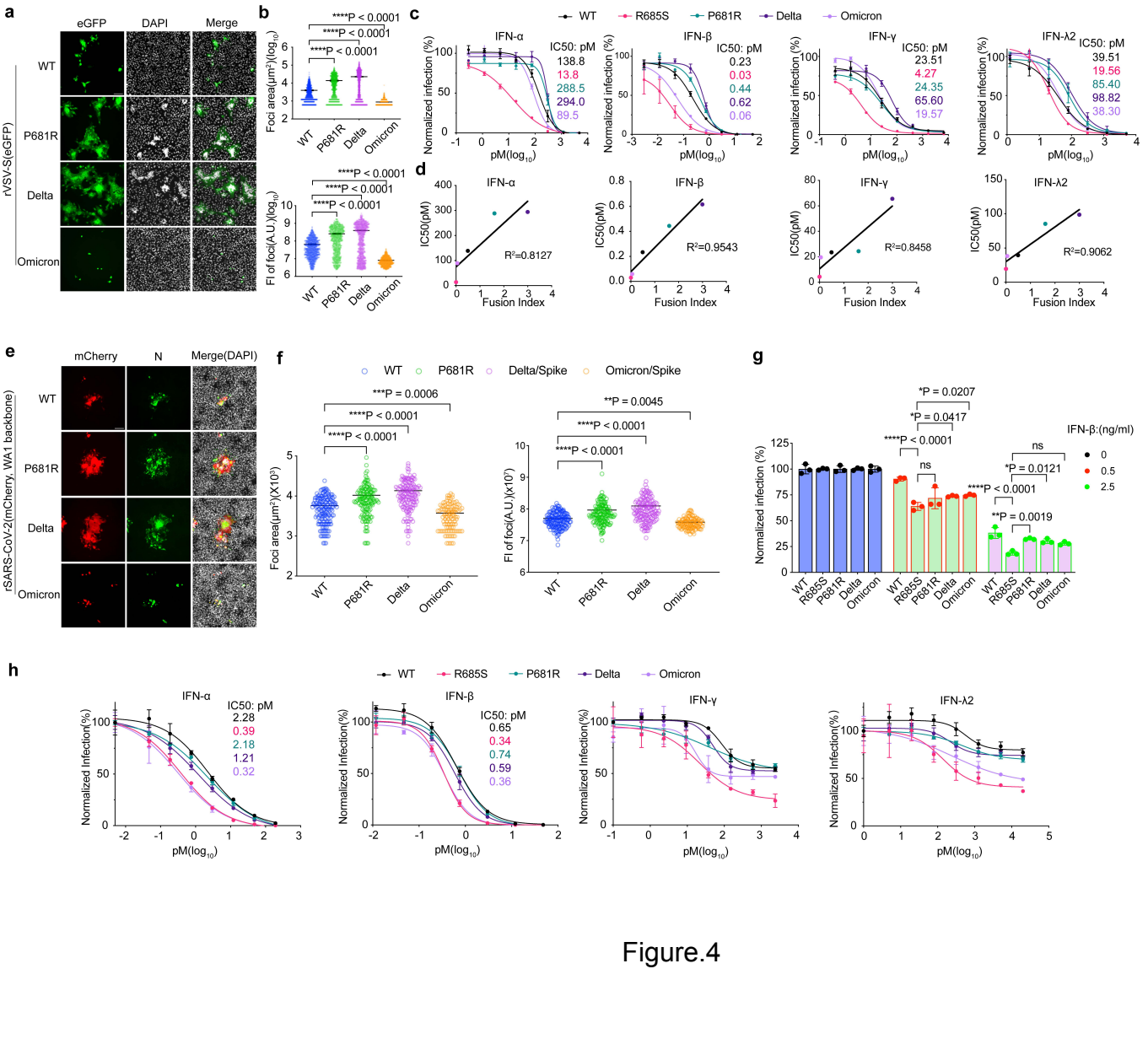
a
eGFP
DAPI
Merge
rVSV-S(eGFP)
WT
P681R
Delta
Omicron
b
****P < 0.0001
****P < 0.0001
****P < 0.0001
Foci area(μm²)(log10)
WT
P681R
Delta
Omicron
****P < 0.0001
****P < 0.0001
****P < 0.0001
FI of foci(A.U.)(log10)
c
WT
R685S
P681R
Delta
Omicron
IFN-α
IC50: pM
138.8
13.8
288.5
294.0
89.5
IFN-β
IC50: pM
0.23
0.03
0.44
0.62
0.06
IFN-γ
IC50: pM
23.51
4.27
24.35
65.60
19.57
IFN-λ2
IC50: pM
39.51
19.56
85.40
98.82
38.30
Normalized infection (%)
pM(log10)
d
IFN-α
R²=0.8127
IFN-β
R²=0.9543
IFN-γ
R²=0.8458
IFN-λ2
R²=0.9062
IC50(pM)
Fusion Index
e
mCherry
N
Merge(DAPI)
rSARS-CoV-2(mCherry, WA1 backbone)
WT
P681R
Delta
Omicron
f
WT
P681R
Delta/Spike
Omicron/Spike
***P = 0.0006
****P < 0.0001
****P < 0.0001
Foci area(μm²)(X10³)
**P = 0.0045
****P < 0.0001
****P < 0.0001
FI of foci(A.U.)(x10⁷)
g
*P = 0.0207
*P = 0.0417
****P < 0.0001
ns
*P = 0.0121
****P < 0.0001
**P = 0.0019
ns
IFN-β:(ng/ml)
0
0.5
2.5
Normalized infection (%)
WT
R685S
P681R
Delta
Omicron
h
WT
R685S
P681R
Delta
Omicron
IFN-α
IC50: pM
2.28
0.39
2.18
1.21
0.32
IFN-β
IC50: pM
0.65
0.34
0.74
0.59
0.36
IFN-γ
IFN-λ2
Normalized Infection(%)
pM(log10)

Figure.4

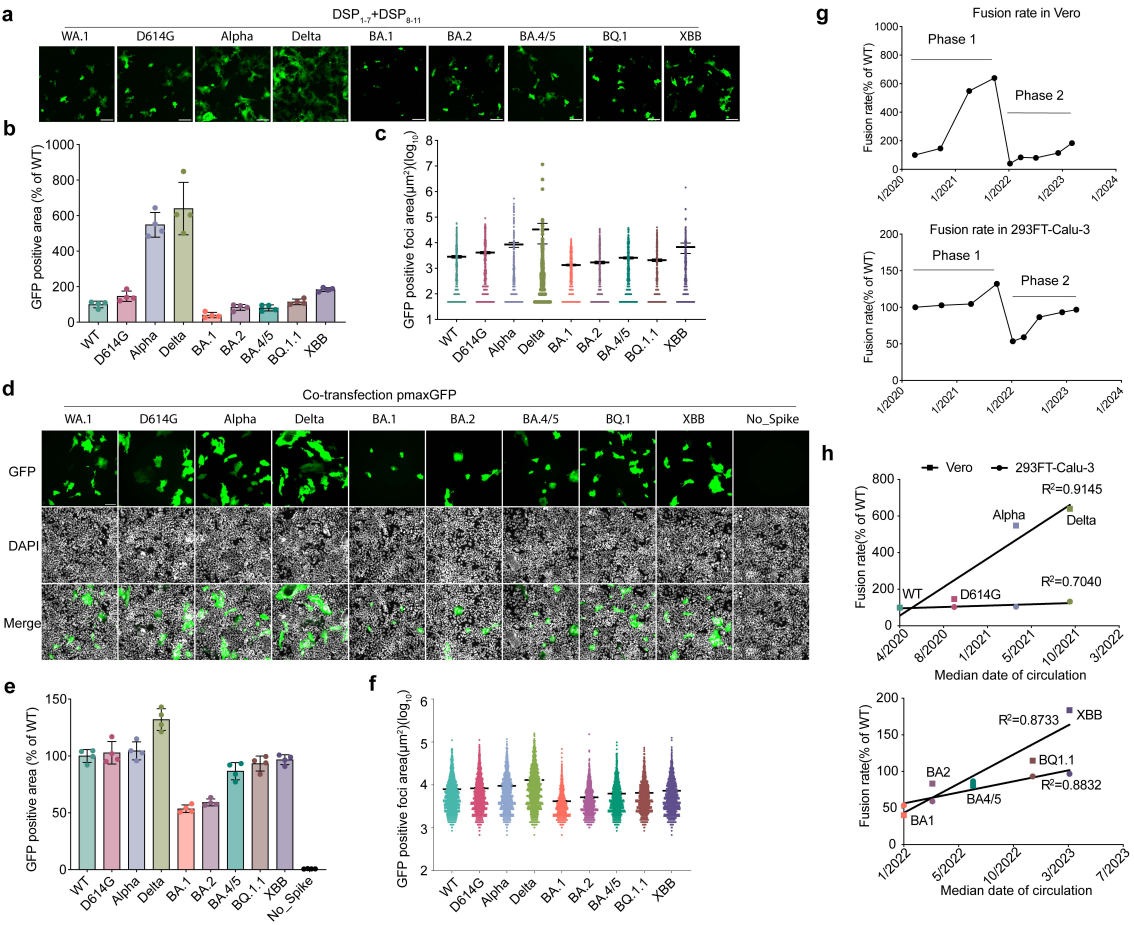
a
DSP1-7+DSP8-11
WA.1
D614G
Alpha
Delta
BA.1
BA.2
BA.4/5
BQ.1
XBB
b
GFP positive area (% of WT)
c
GFP positive foci area(μm²)/(log10)
d
Co-transfection pmaxGFP
No_Spike
GFP
DAPI
Merge
e
f
g
Fusion rate in Vero
Phase 1
Phase 2
Fusion rate(% of WT)
Fusion rate in 293FT-Calu-3
h
Vero
293FT-Calu-3
R²=0.9145
R²=0.7040
R²=0.8733
R²=0.8832
Median date of circulation

Figure.5

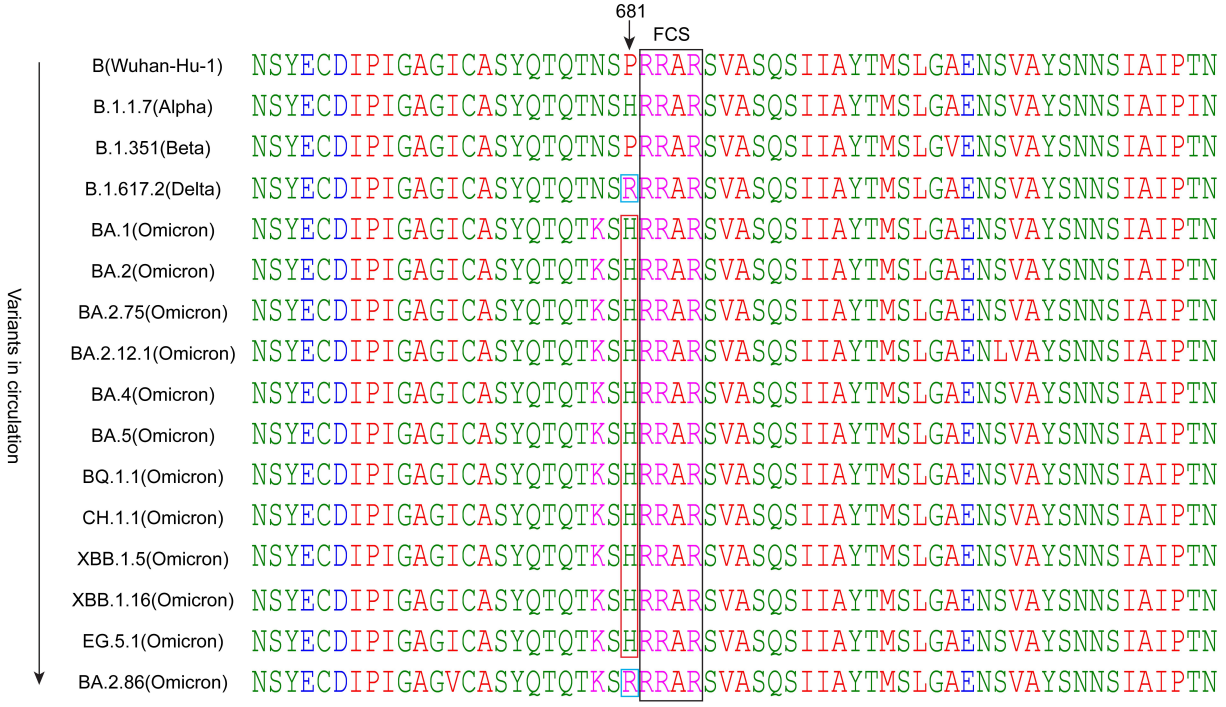
681
FCS
Variants in circulation
B(Wuhan-Hu-1) NSYECDIPIGAGICASYQTQTNSPRRARSVASQSIIAYTMSLGAENSVAYSNNSIAIPTN
B.1.1.7(Alpha) NSYECDIPIGAGICASYQTQTNSHRRARSVASQSIIAYTMSLGAENSVAYSNNSIAIPIN
B.1.351(Beta) NSYECDIPIGAGICASYQTQTNSPRRARSVASQSIIAYTMSLGVENSVAYSNNSIAIPTN
B.1.617.2(Delta) NSYECDIPIGAGICASYQTQTNSRRRARSVASQSIIAYTMSLGAENSVAYSNNSIAIPTN
BA.1(Omicron) NSYECDIPIGAGICASYQTQTKSHRRARSVASQSIIAYTMSLGAENSVAYSNNSIAIPTN
BA.2(Omicron) NSYECDIPIGAGICASYQTQTKSHRRARSVASQSIIAYTMSLGAENSVAYSNNSIAIPTN
BA.2.75(Omicron) NSYECDIPIGAGICASYQTQTKSHRRARSVASQSIIAYTMSLGAENSVAYSNNSIAIPTN
BA.2.12.1(Omicron) NSYECDIPIGAGICASYQTQTKSHRRARSVASQSIIAYTMSLGAENLVAYSNNSIAIPTN
BA.4(Omicron) NSYECDIPIGAGICASYQTQTKSHRRARSVASQSIIAYTMSLGAENSVAYSNNSIAIPTN
BA.5(Omicron) NSYECDIPIGAGICASYQTQTKSHRRARSVASQSIIAYTMSLGAENSVAYSNNSIAIPTN
BQ.1.1(Omicron) NSYECDIPIGAGICASYQTQTKSHRRARSVASQSIIAYTMSLGAENSVAYSNNSIAIPTN
CH.1.1(Omicron) NSYECDIPIGAGICASYQTQTKSHRRARSVASQSIIAYTMSLGAENSVAYSNNSIAIPTN
XBB.1.5(Omicron) NSYECDIPIGAGICASYQTQTKSHRRARSVASQSIIAYTMSLGAENSVAYSNNSIAIPTN
XBB.1.16(Omicron) NSYECDIPIGAGICASYQTQTKSHRRARSVASQSIIAYTMSLGAENSVAYSNNSIAIPTN
EG.5.1(Omicron) NSYECDIPIGAGICASYQTQTKSHRRARSVASQSIIAYTMSLGAENSVAYSNNSIAIPTN
BA.2.86(Omicron) NSYECDIPIGAGVCASYQTQTKSRRRARSVASQSIIAYTMSLGAENSVAYSNNSIAIPTN

Figure.S1

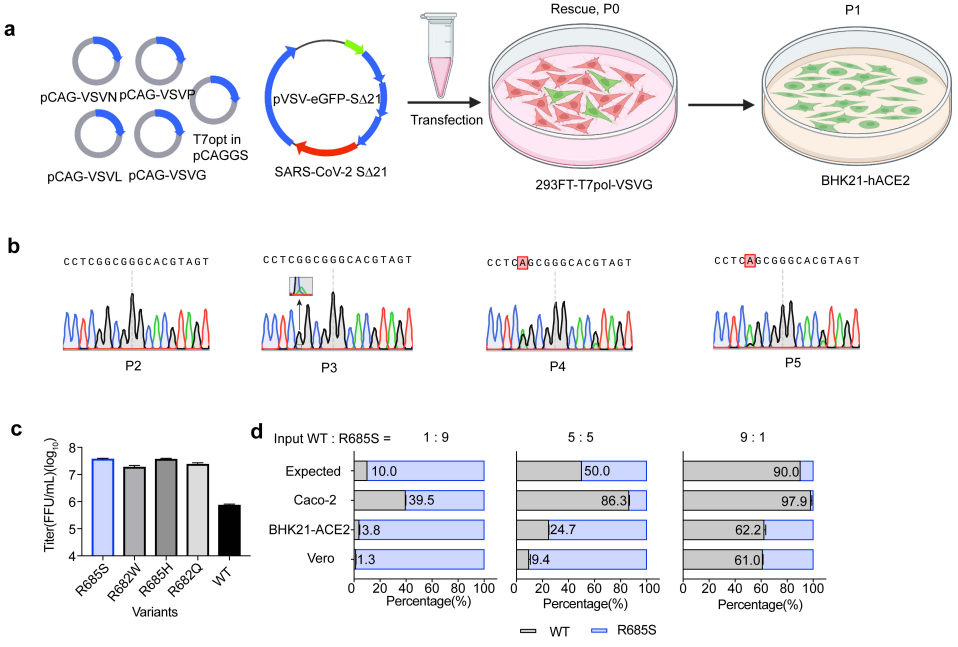
a
pCAG-VSVN
pCAG-VSVP
T7opt in pCAGGS
pCAG-VSVL
pCAG-VSVG
pVSV-eGFP-SΔ21
SARS-CoV-2 SΔ21
Transfection
Rescue, P0
293FT-T7pol-VSVG
P1
BHK21-hACE2
b
CCTCGGCGGGCACGTAGT
CCTCAGCGGGCACGTAGT
P2
P3
P4
P5
c
Titer(FFU/mL)(log10)
R685S
R682W
R685H
R682Q
WT
Variants
d
Input WT : R685S =
1 : 9
5 : 5
9 : 1
Expected
Caco-2
BHK21-ACE2
Vero
10.0
39.5
3.8
1.3
50.0
86.3
24.7
9.4
90.0
97.9
62.2
61.0
Percentage(%)
WT
R685S

Figure.S2

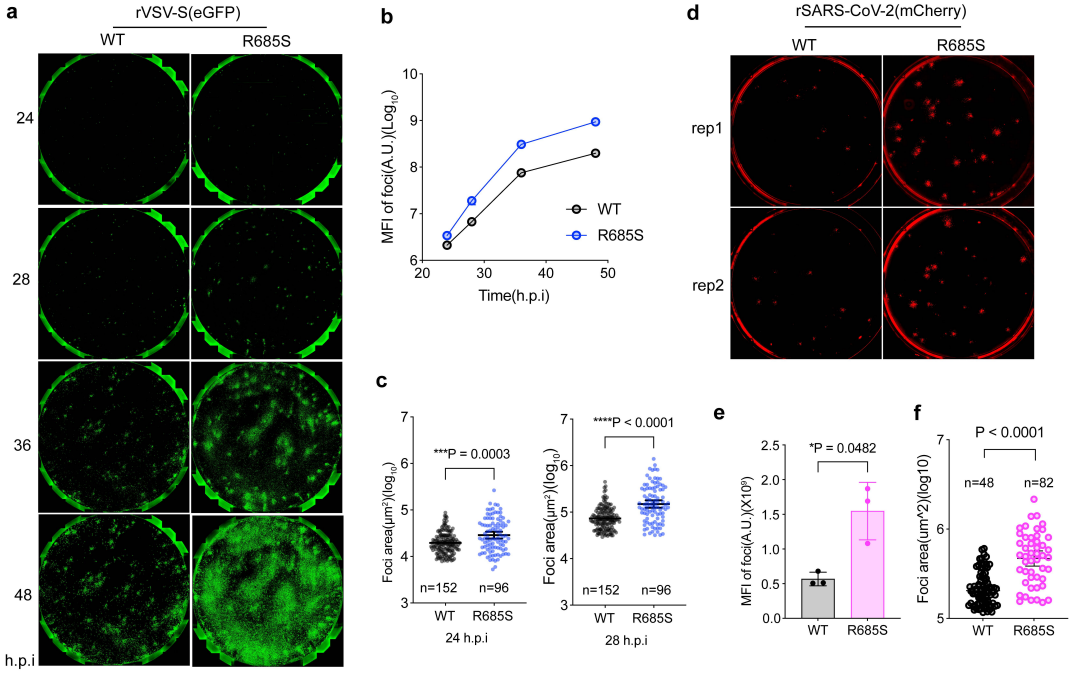
a
rVSV-S(eGFP)
WT
R685S
24
28
36
48
h.p.i
b
MFI of foci(A.U.)(Log10)
Time(h.p.i)
WT
R685S
d
rSARS-CoV-2(mCherry)
WT
R685S
rep1
rep2
c
Foci area(μm²)(log10)
***P = 0.0003
n=152
n=96
WT
R685S
24 h.p.i
****P < 0.0001
28 h.p.i
e
MFI of foci(A.U.)(X10⁸)
*P = 0.0482
f
Foci area(um^2)(log10)
P < 0.0001
n=48
n=82

Figure.S3

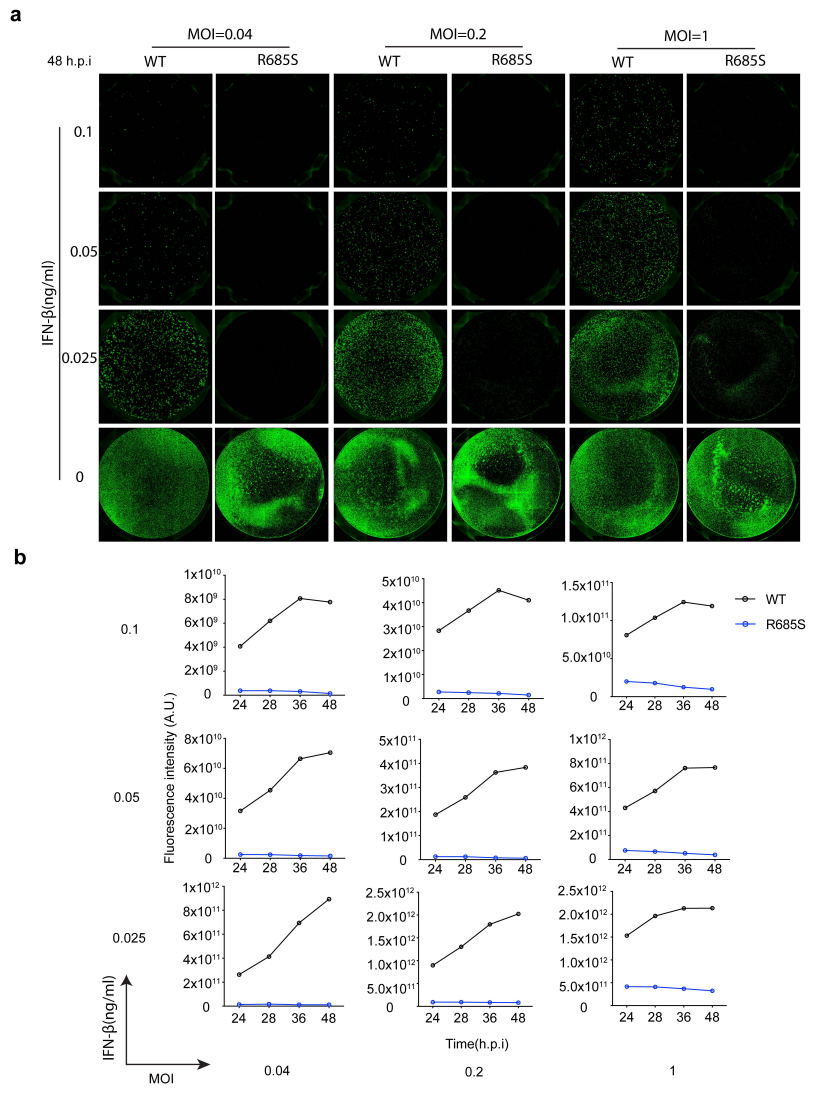
a
MOI=0.04
MOI=0.2
MOI=1
48 h.p.i
WT
R685S
WT
R685S
WT
R685S
IFN-β(ng/ml)
0.1
0.05
0.025
0
b
0.1
0.05
0.025
Fluorescence intensity (A.U.)
WT
R685S
24
28
36
48
IFN-β(ng/ml)
MOI
0.04
0.2
1
Time(h.p.i)

Figure.S4

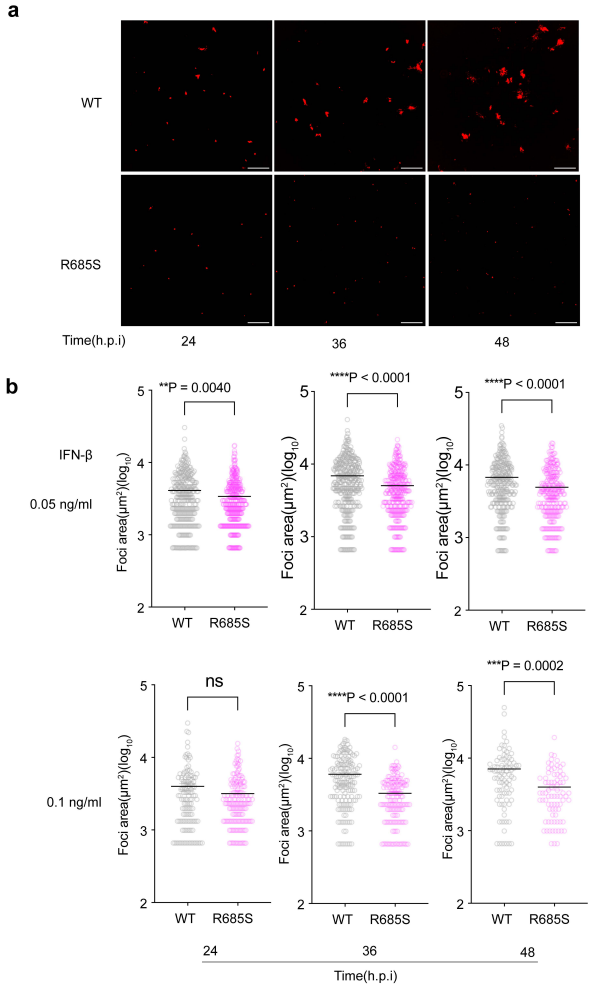
a
WT
R685S
Time(h.p.i)
24
36
48
b
IFN-β
0.05 ng/ml
0.1 ng/ml
**P = 0.0040
****P < 0.0001
****P < 0.0001
ns
****P < 0.0001
***P = 0.0002
Foci area(μm²)(log10)
WT
R685S
24
36
48
Time(h.p.i)

Figure.S5

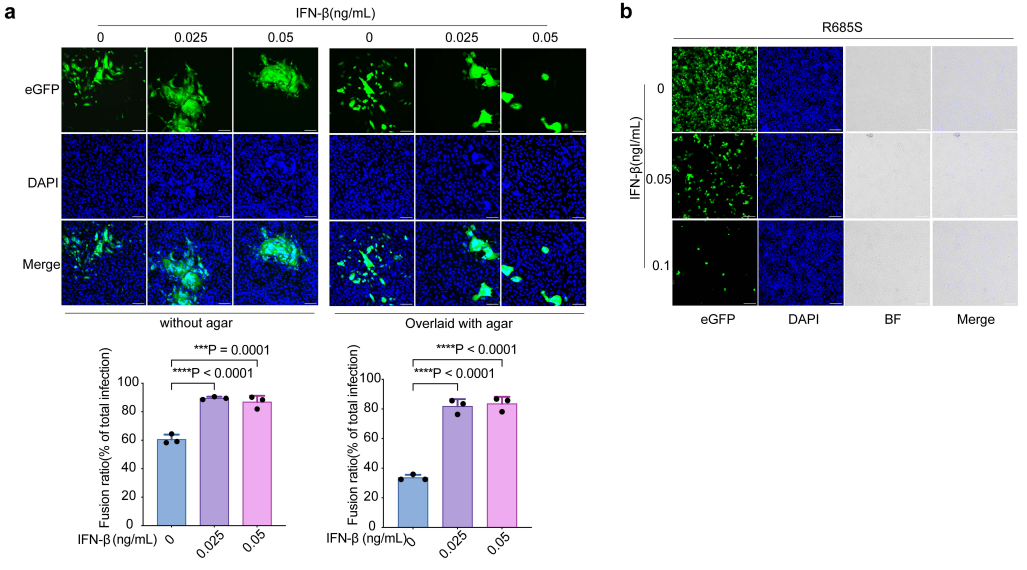
a
IFN-β(ng/mL)
0
0.025
0.05
0
0.025
0.05
eGFP
DAPI
Merge
without agar
Overlaid with agar
***P = 0.0001
****P < 0.0001
Fusion ratio(% of total infection)
IFN-β (ng/mL)
b
R685S
IFN-β(ng/mL)
0
0.05
0.1
eGFP
DAPI
BF
Merge

Figure.S6

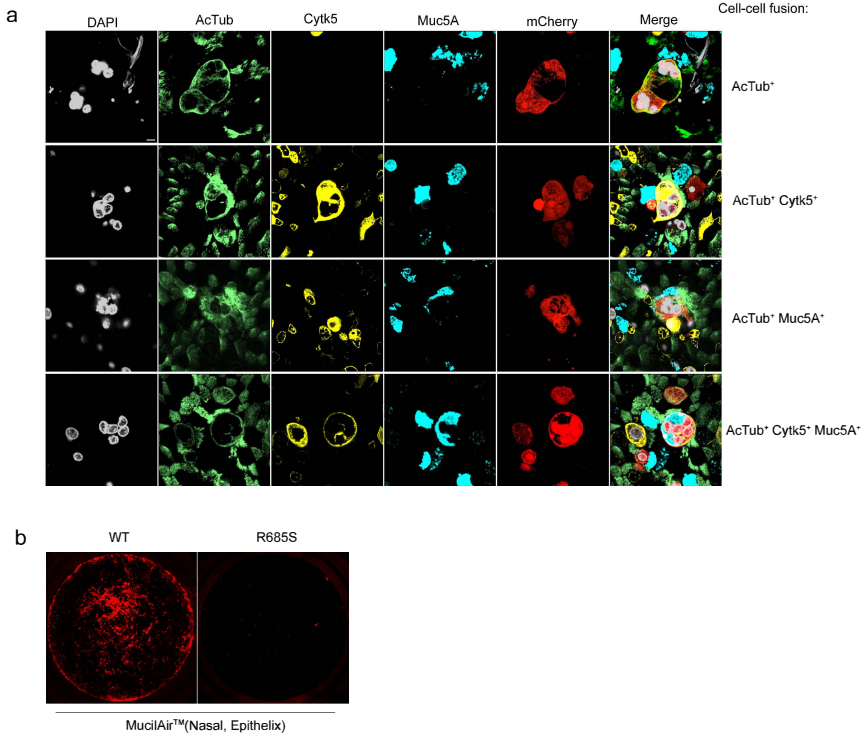
a
DAPI
AcTub
Cytk5
Muc5A
mCherry
Merge
Cell-cell fusion:
AcTub+
AcTub+ Cytk5+
AcTub+ Muc5A+
AcTub+ Cytk5+ Muc5A+
b
WT
R685S
MucilAir™(Nasal, Epithelix)

Figure.S7

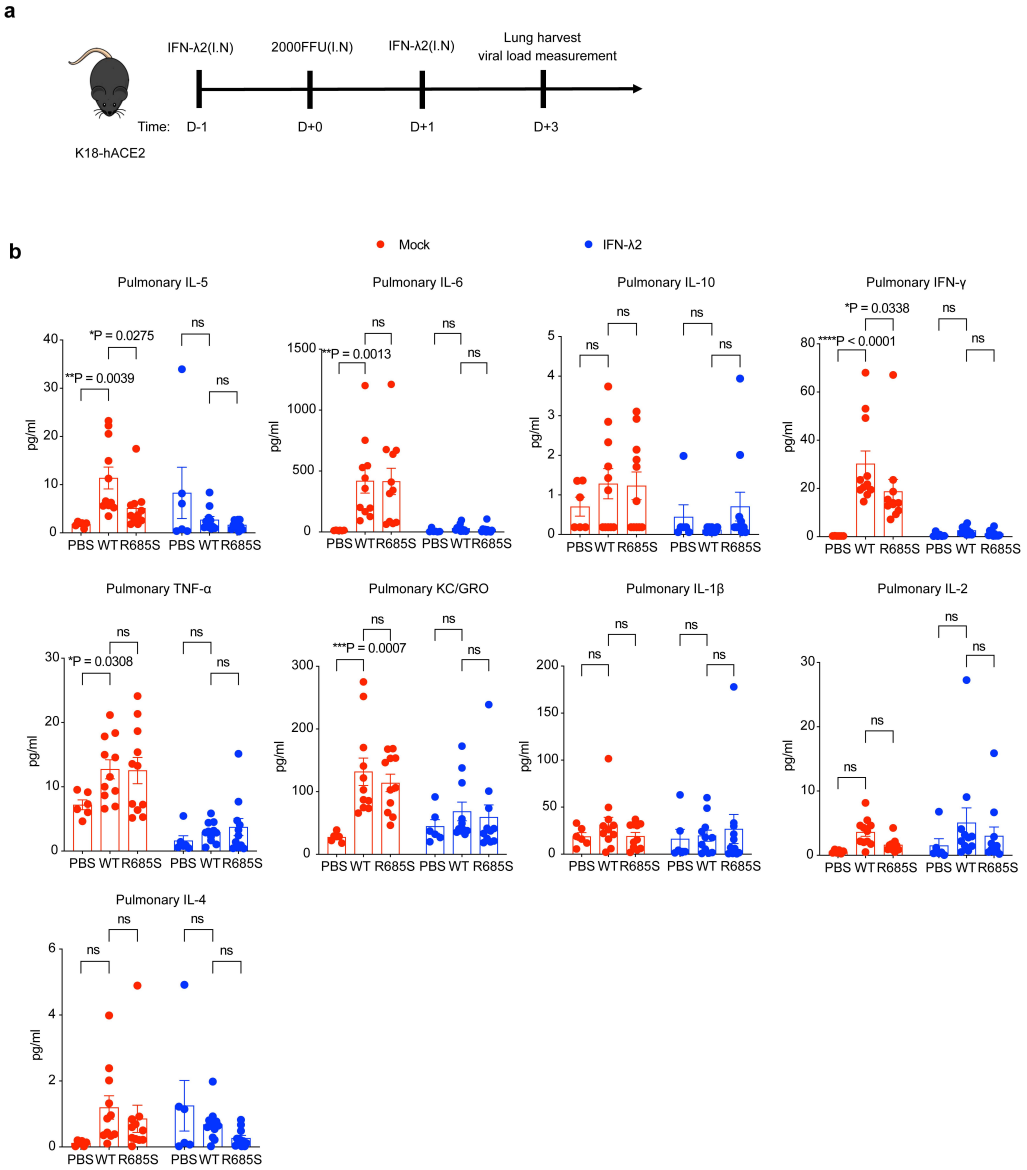
a
IFN-λ2(I.N)
2000FFU(I.N)
IFN-λ2(I.N)
Lung harvest
viral load measurement
Time:
D-1
D+0
D+1
D+3
K18-hACE2
b
Mock
IFN-λ2
Pulmonary IL-5
Pulmonary IL-6
Pulmonary IL-10
Pulmonary IFN-γ
Pulmonary TNF-α
Pulmonary KC/GRO
Pulmonary IL-1β
Pulmonary IL-2
Pulmonary IL-4
pg/ml
*P = 0.0275
**P = 0.0039
**P = 0.0013
*P = 0.0338
****P < 0.0001
*P = 0.0308
***P = 0.0007
ns
PBS WT R685S PBS WT R685S

Figure.S8

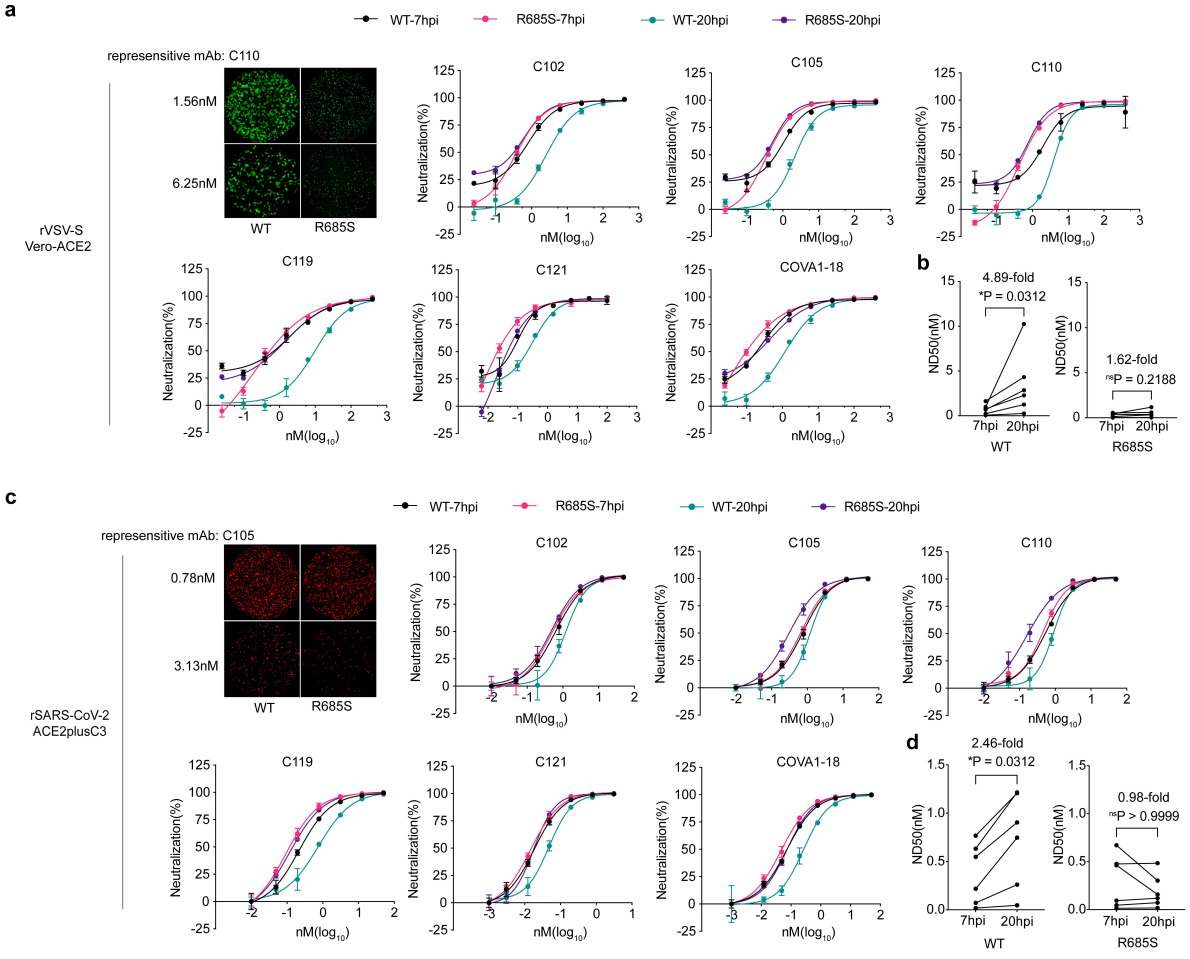
a
WT-7hpi
R685S-7hpi
WT-20hpi
R685S-20hpi
represensitive mAb: C110
1.56nM
6.25nM
WT
R685S
rVSV-S
Vero-ACE2
C102
C105
C110
C119
C121
COVA1-18
Neutralization(%)
nM(log10)
b
4.89-fold
*P = 0.0312
1.62-fold
nsP = 0.2188
ND50(nM)
7hpi
20hpi
c
represensitive mAb: C105
0.78nM
3.13nM
rSARS-CoV-2
ACE2plusC3
d
2.46-fold
*P = 0.0312
0.98-fold
nsP > 0.9999

Figure.S9

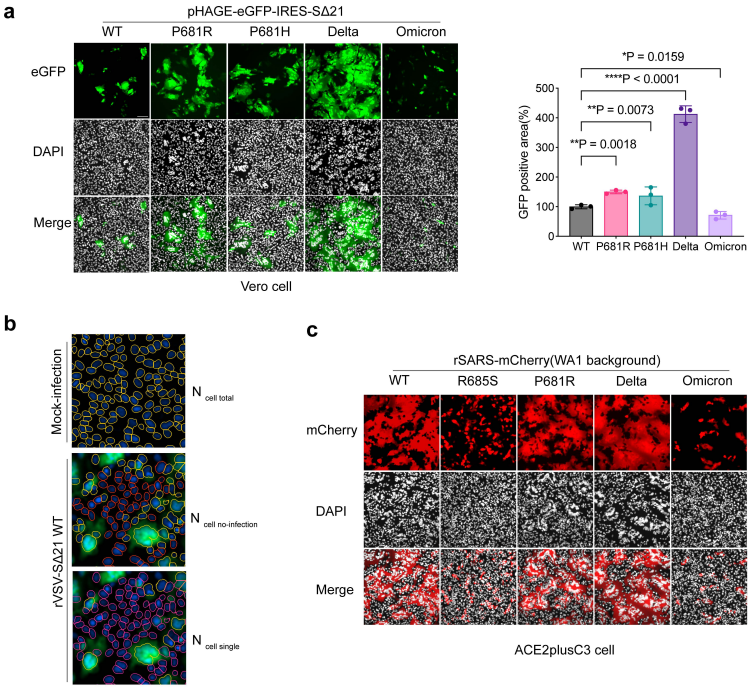
a
pHAGE-eGFP-IRES-SΔ21
WT
P681R
P681H
Delta
Omicron
eGFP
DAPI
Merge
Vero cell
*P = 0.0159
****P < 0.0001
**P = 0.0073
**P = 0.0018
GFP positive area(%)
500
400
300
200
100
0
WT P681R P681H Delta Omicron
b
Mock-infection
rVSV-SΔ21 WT
N cell total
N cell no-infection
N cell single
c
rSARS-mCherry(WA1 background)
WT
R685S
P681R
Delta
Omicron
mCherry
DAPI
Merge
ACE2plusC3 cell

Figure.S10

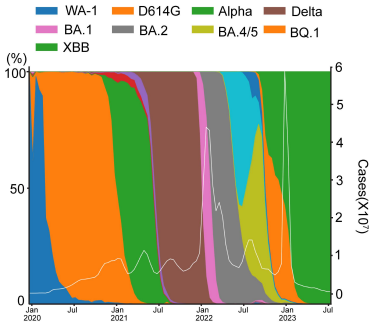
WA-1
D614G
Alpha
Delta
BA.1
BA.2
BA.4/5
BQ.1
XBB
(%)
100
50
0
6
5
4
3
2
1
0
Cases(X10⁷)
Jan 2020
Jul
Jan 2021
Jul
Jan 2022
Jul
Jan 2023
Jul

Figure.S11